PHYSICAL REVIEW D **92,** 054511 (2015)

Nucleon electromagnetic form factors in two-flavor QCD

S. Capitani,[1,2] M. Della Morte,[3] D. Djukanovic,[2] G. von Hippel,[1] J. Hua,[1] B. Jäger,[4] B. Knippschild,[1,*] H. B. Meyer,[1,2] T. D. Rae,[1,†] and H. Wittig[1,2,‡]

[1]*PRISMA Cluster of Excellence and Institut für Kernphysik, University of Mainz, Becher-Weg 45, 55099 Mainz, Germany*

[2]*Helmholtz Institute Mainz, University of Mainz, 55099 Mainz, Germany*

[3]*CP3-Origins, University of Southern Denmark, Campusvej 55, 5230 Odense M, Denmark*

[4]*Department of Physics, College of Science, Swansea University, Swansea SA2 8PP, United Kingdom*

(Received 28 April 2015; published 25 September 2015)

We present results for the nucleon electromagnetic form factors, including the momentum transfer dependence and derived quantities (charge radii and magnetic moment). The analysis is performed using $\mathcal{O}(a)$ improved Wilson fermions in $N_f = 2$ QCD measured on the Coordinated Lattice Simulations ensembles. Particular focus is placed on a systematic evaluation of the influence of excited states in three-point correlation functions, which lead to a biased evaluation, if not accounted for correctly. We argue that the use of summed operator insertions and fit Ansätze including excited states allow us to suppress and control this effect. We employ a novel method to perform joint chiral and continuum extrapolations, by fitting the form factors directly to the expressions of covariant baryonic chiral effective field theory. The final results for the charge radii and magnetic moment from our lattice calculations include, for the first time, a full error budget. We find that our estimates are compatible with experimental results within their overall uncertainties.

DOI: 10.1103/PhysRevD.92.054511 PACS numbers: 12.38.Gc, 13.40.Gp, 14.20.Dh

I. INTRODUCTION

The electromagnetic form factors, G_E and G_M, of the nucleon encode information on the distribution of charge and magnetization and are among the key quantities describing its internal structure. Experimental measurements of these quantities in ep scattering processes have a long history (see, e.g., the review [1]) and have been pushed to ever higher precision [2,3]. In spite of the fact that nucleon electromagnetic form factors have been studied extensively in theory and experiment, there are several open questions. The first concerns the deviation between the ratio G_E/G_M as determined using the traditional Rosenbluth separation technique and the result obtained from recoil polarization [4–7] at squared momentum transfers Q^2 larger than 1 GeV^2. Second, prompted by the observed discrepancy between the proton charge radius extracted from the Lamb shift in muonic hydrogen [8,9] and the value obtained by using the electron as a probe [3,10], there is a strong interest in new experimental measurements of form factors in the regime of very small Q^2, as well as in further theoretical studies, in order to reduce the inherent systematics. The third open issue concerns our understanding of the internal structure of the nucleon in terms of the underlying gauge theory of QCD. Nucleon form factors have been studied extensively in simulations of QCD on a space-time lattice [11–23], and although these calculations are quite straightforward, they mostly fail in reproducing the experimentally observed Q^2-dependence of G_E and G_M. As a consequence, lattice estimates for the electric charge radius derived from the slope of G_E at vanishing Q^2 are typically underestimated compared to the results derived from ep scattering data. It is widely believed that systematic errors in lattice calculations must be held responsible for this deviation.

In addition to systematic errors induced by nonzero lattice spacings, finite volumes, and uncertainties associated with the chiral extrapolation, the issue of contamination from excited states in calculations of nucleon correlation functions has recently come to the fore as a possible explanation for the deviation between experimental and lattice estimates of the electric charge radius.

In this paper we present a detailed investigation of systematic effects in lattice calculations of nucleon form factors arising from excited-state contributions. In particular, we apply the technique of summed operator insertions [24–26] which has proven very useful in our earlier calculation of the axial charge of the nucleon [27]. Furthermore, we address in detail the chiral extrapolation to the physical pion mass, by employing several variants of baryonic chiral perturbation theory (ChPT).

Our simulations are performed in two-flavor QCD with a mass-degenerate doublet of up and down quarks. Since excited-state contamination is an issue for lattice simulations with any number of dynamical quarks, the question whether estimates for nucleon charge radii and

*Present address: Helmholtz-Institut für Strahlen- und Kernphysik (Theorie), Universität Bonn, 53115 Bonn, Germany.

†thrae@uni-mainz.de

Present address: Bergische Universität Wuppertal, Gaussstr. 20, D-42119 Wuppertal, Germany.

‡hartmut.wittig@uni-mainz.de

magnetic moments may be biased can be adequately addressed in this setup. There is ample evidence [28] that there are no discernible differences between QCD with $N_f = 2$ and $N_f = 2 + 1$ flavors at the few-percent level. Therefore, the observed deviation between lattice QCD and the experiment is far too large to be explained by the presence or absence of a dynamical strange quark.

Our central findings include the observation that excited-state contaminations have a sizeable influence on the form factors extracted from the still widely used plateau method applied to ratios of three- and two-point functions at least up to source-sink separations of ∼1.5 fm. The use of summed insertions, while generally an important tool in suppressing excited-state effects on hadron structure quantities, cannot reliably exclude a residual bias, in particular when comparing with the results of fits which include excited states explicitly. Moreover, for the first time, we apply the full framework of covariant baryonic chiral perturbation theory [29–32] to the simultaneous determination of the form factors near $Q^2 = 0$ and at the physical pion mass. From a careful study of all relevant systematic effects, we are able to give a full error budget. Our final results for various charge radii and the anomalous magnetic moments κ are listed in Eq. (34) below. We observe agreement with experiment within the accuracy of our calculation, including systematic errors. However, the overall uncertainty is too large to have an impact on the proton radius puzzle.

This paper is organized as follows. In Sec. II, we describe our lattice setup, including details of the ensembles used and observables measured, as well as our evaluation of statistical errors. In Sec. III, we discuss the analysis methods we employed to study and suppress excited-state contributions. The Q^2-dependence of the measured form factors, and the values of the charge radii and magnetic moment determined from dipole fits on each ensemble, are presented in Sec. IV. In Sec. V, we discuss in detail the chiral fits to the form factors which we use to obtain our final results. Section VI contains our conclusions and a brief outlook.

A discussion of the impact of the use of Lorentz-noncovariant interpolating operators obtained from smearing the quark fields in the spatial directions only on the Lorentz invariance of the results so obtained is contained in Appendix A. For ease of reference, we provide tables containing the full set of our results for the form factors at all values of Q^2 on all ensembles in Appendix B.

II. LATTICE SETUP

A. Observables and correlators

The matrix element of the electromagnetic current

$$V^{\mu}_{\mathrm{em}} = \frac{2}{3}\bar{u}\gamma^{\mu}u - \frac{1}{3}\bar{d}\gamma^{\mu}d + \ldots \tag{1}$$

between one-nucleon states can be expressed in terms of the Dirac and Pauli form factors, F_1 and F_2. In Minkowski space notation, the form factor decomposition reads

$$\langle N(p',s')|V^{\mu}_{\mathrm{em}}(0)|N(p,s)\rangle = \bar{u}(p',s')\left[\gamma^{\mu}F_1(q^2) + i\frac{\sigma^{\mu\nu}q_{\nu}}{2m_{\mathrm{N}}}F_2(q^2)\right]u(p,s), \tag{2}$$

where $u(p,s)$ is a Dirac spinor with spin s and momentum p, γ^{μ} is a Dirac matrix, $\sigma^{\mu\nu} = \frac{i}{2}[\gamma^{\mu},\gamma^{\nu}]$, and m_{N} denotes the nucleon mass.

The four-momentum transfer $q \equiv p' - p$ is expressed in terms of the energies and three-momenta of the initial and final states as

$$q^2 = -Q^2 = (E_{\boldsymbol{p}'} - E_{\boldsymbol{p}})^2 - (\boldsymbol{p}' - \boldsymbol{p})^2. \tag{3}$$

In this paper, we focus on the isovector form factors. By assuming isospin symmetry, one can show via a simple application of the Wigner–Eckart theorem applied in isospin space that

$$\langle \mathrm{p}(p',s')|\bar{u}\gamma^{\mu}u - \bar{d}\gamma^{\mu}d|\mathrm{p}(p,s)\rangle = \langle \mathrm{p}(p',s')|V^{\mu}_{\mathrm{em}}|\mathrm{p}(p,s)\rangle - \langle \mathrm{n}(p',s')|V^{\mu}_{\mathrm{em}}|\mathrm{n}(p,s)\rangle, \tag{4}$$

where $|\mathrm{p}\rangle$ and $|\mathrm{n}\rangle$ refer to one-proton and one-neutron states, respectively. The expression on the left-hand side is suitable for lattice QCD calculations, while the right-hand side allows one to compare the results to experimental measurements.

The Dirac and Pauli form factors give rise to the helicity-preserving and helicity-flipping contributions to the amplitude, respectively. The electric and magnetic (Sachs) form factors G_{E} and G_{M} are obtained as linear combinations of F_1 and F_2,

$$G_{\mathrm{E}}(q^2) = F_1(q^2) + \frac{q^2}{4m_N^2}F_2(q^2), \tag{5}$$

$$G_{\mathrm{M}}(q^2) = F_1(q^2) + F_2(q^2). \tag{6}$$

They can be determined from ep scattering experiments by decomposing the measured differential cross section through the Rosenbluth formula [33]. The form factors may be Taylor expanded in the squared momentum transfer q^2,

$$G_{\mathrm{E,M}}(q^2) = G_{\mathrm{E,M}}(0)\left(1 + \frac{1}{6}\langle r^2_{\mathrm{E,M}}\rangle q^2 + \mathcal{O}(q^4)\right), \tag{7}$$

from which the charge radii of the nucleon may be determined:

$$\langle r^2_{\mathrm{E,M}}\rangle = \frac{6}{G_{\mathrm{E,M}}(q^2)}\frac{\partial G_{\mathrm{E,M}}(q^2)}{\partial q^2}\bigg|_{q^2=0}. \tag{8}$$

Electric charge conservation implies $G_{\mathrm{E}}(0)=1$, while the magnetic moment μ of the nucleon, in units of the nuclear magneton $e/2m_{\mathrm{N}}$, is obtained from the magnetic form factor at vanishing q^2, $G_{\mathrm{M}}(0)=\mu$.

Lattice simulations allow for the determination of hadronic matrix elements by computing Euclidean correlation functions of local composite operators.[1] To this end, one considers the nucleon two-point function

$$C_2(\boldsymbol{p},t) = \sum_{\boldsymbol{x}} \mathrm{e}^{i\boldsymbol{p}\cdot\boldsymbol{x}}\Gamma_{\beta\alpha}\langle\Psi^{\alpha}(\boldsymbol{x},t)\bar{\Psi}^{\beta}(0)\rangle, \tag{9}$$

where $\Psi^{\alpha}(\boldsymbol{x},t)$ denotes a standard interpolating operator for the nucleon and Γ is a projection matrix in spinor space. In this work, the kinematics is chosen such that the final nucleon is at rest, i.e. $\boldsymbol{p}'=0$. Hence, the three-momentum transfer $\boldsymbol{q}\equiv\boldsymbol{p}'-\boldsymbol{p}$ is given by

$$\boldsymbol{q} = -\boldsymbol{p}, \tag{10}$$

and the expression for the three-point function of a generic (Euclidean) vector current V_μ reads

$$C_{3,V_\mu}(\boldsymbol{q},t,t_s) = \sum_{\boldsymbol{x}\boldsymbol{y}} \mathrm{e}^{i\boldsymbol{q}\cdot\boldsymbol{y}}\Gamma_{\beta\alpha}\langle\Psi^{\alpha}(\boldsymbol{x},t_s)V_\mu(\boldsymbol{y},t)\bar{\Psi}^{\beta}(0)\rangle. \tag{11}$$

For the nucleon correlation functions considered in this work, the projection matrix

$$\Gamma = \frac{1}{2}(1+\gamma_0)(1+i\gamma_5\gamma_3) \tag{12}$$

ensures the correct parity of the created states and gives the nucleon a polarization in the z-direction, which is required to extract the magnetic form factor. In the above expression for the three-point function, the vector current is inserted at Euclidean time t, while the Euclidean time separation between the initial and final nucleons is denoted by t_s. Figure 1 shows the corresponding diagrams of the two- and three-point functions. Note that for the isovector vector current considered in this work quark-disconnected diagrams cancel.

The electric and magnetic form factors are easily determined from suitable ratios of correlation functions. Here, we follow Ref. [34] and use the ratio found to be most effective in isolating the desired matrix element. For our chosen kinematics, it reads

[1]From here on, we use Euclidean notation for the position- and momentum-space vectors, as well as for the Dirac matrices.

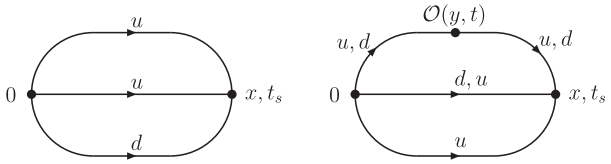

FIG. 1. Baryonic two-point and three-point functions (left and right panels, respectively).

$$R_{V_\mu}(\boldsymbol{q},t,t_s) = \frac{C_{3,V_\mu}(\boldsymbol{q},t,t_s)}{C_2(\boldsymbol{0},t_s)}\sqrt{\frac{C_2(\boldsymbol{q},t_s-t)C_2(\boldsymbol{0},t)C_2(\boldsymbol{0},t_s)}{C_2(\boldsymbol{0},t_s-t)C_2(\boldsymbol{q},t)C_2(\boldsymbol{q},t_s)}}. \tag{13}$$

From the asymptotic behavior of $R_{V_\mu}(\boldsymbol{q},t,t_s)$, one can then extract G_{E} and G_{M} for spacelike momenta $Q^2\equiv -q^2>0$ via

$$R_{V_0}(\boldsymbol{q},t,t_s) \overset{t,(t_s-t)\gg 0}{\longrightarrow} \sqrt{\frac{m_N+E_{\boldsymbol{q}}}{2E_{\boldsymbol{q}}}}G^{\mathrm{bare}}_{\mathrm{E}}(Q^2), \tag{14}$$

and

$$\mathrm{Re}R_{V_i}(\boldsymbol{q},t,t_s) \overset{t,(t_s-t)\gg 0}{\longrightarrow} \epsilon_{ij3}q_j\sqrt{\frac{1}{2E_{\boldsymbol{q}}(E_{\boldsymbol{q}}+m_N)}}G^{\mathrm{bare}}_{\mathrm{M}}(Q^2), \tag{15}$$

where the ϵ symbol in the last equation denotes the antisymmetric tensor with $\epsilon_{123}=+1$ and the superscripts "bare" remind us that, in general, the vector current requires renormalization in the lattice-regularized theory.

B. Simulation details

Our calculations have been performed on a set of ensembles with $N_f=2$ flavors of $\mathcal{O}(a)$-improved Wilson quarks and the Wilson plaquette action. For the improvement coefficient c_{sw}, we used the nonperturbative determination of Ref. [35]. The gauge configurations have been generated as part of the Coordinated Lattice Simulations (CLS) initiative, using the deflation-accelerated DD-HMC [36,37] and MP-HMC [38] algorithms. Table I provides details of the lattice ensembles used.

For the calculation of three-point correlation functions, we employed the point-split isovector current

$$V^{\mathrm{con}}_{\mu}(x) = \frac{1}{2}(\bar{\psi}(x+\hat{\mu})(1+\gamma_\mu)U^{\dagger}_{\mu}(x)\tau^3\psi(x) - \bar{\psi}(x)(1-\gamma_\mu)U_\mu(x)\tau^3\psi(x+\hat{\mu})) \tag{16}$$

as well as the local vector current

$$V^{\mathrm{loc}}_{\mu}(x) = \bar{\psi}(x)\gamma_\mu\tau^3\psi(x). \tag{17}$$

TABLE I. Details of the lattice ensembles used in this study, showing the lattice extent, L, where $T = 2L$; the values of the bare parameters β and κ in the lattice action; the pion and nucleon masses (am_π and am_N); the number of measurements, $N_{\mathrm{meas}} = N_{\mathrm{cfg}} \times N_{\mathrm{src}}$; the lattice spacing, a; the pion mass, m_π, in physical units, and the ratio m_π/m_N of the pion and nucleon masses.

Run	L/a	β	κ	am_π	am_N	$m_\pi L$	N_{cfg}	N_{meas}	a (fm)	m_π (MeV)	m_π/m_N
*A*3	32	5.20	0.13580	0.1893(6)	0.546(7)	6.0	133	2128	0.079	473	0.346(5)
*A*4	32	5.20	0.13590	0.1459(7)	0.488(13)	4.7	200	3200	0.079	364	0.299(7)
*A*5	32	5.20	0.13594	0.1265(8)	0.468(7)	4.0	250	4000	0.079	316	0.270(5)
*B*6	48	5.20	0.13597	0.1073(7)	0.444(5)	5.0	159	2544	0.079	268	0.242(3)
*E*5	32	5.30	0.13625	0.1458(3)	0.441(4)	4.7	1000	4000	0.063	457	0.330(3)
*F*6	48	5.30	0.13635	0.1036(3)	0.382(4)	5.0	300	3600	0.063	324	0.271(3)
*F*7	48	5.30	0.13638	0.0885(3)	0.367(5)	4.2	250	3000	0.063	277	0.241(4)
*G*8	64	5.30	0.13642	0.0617(3)	0.352(6)	4.0	348	4176	0.063	193	0.175(3)
*N*5	48	5.50	0.13660	0.1086(2)	0.329(2)	5.2	477	1908	0.050	429	0.330(2)
*N*6	48	5.50	0.13667	0.0838(2)	0.297(3)	4.0	946	3784	0.050	331	0.283(3)
*O*7	64	5.50	0.13671	0.0660(1)	0.271(4)	4.4	490	1960	0.050	261	0.244(3)

Here, ψ denotes an isospin doublet of up- and down-quark fields, and τ^3 is the Pauli matrix acting in isospin space. While the point-split current is conserved and satisfies the corresponding Ward identity, the local vector current must be renormalized. The expression for the renormalized current in the $\mathcal{O}(a)$ improved theory reads [39]

$$V_\mu^{\mathrm{R}} = Z_{\mathrm{V}}(1 + b_{\mathrm{V}} a m_{\mathrm{q}})(V_\mu^{\mathrm{loc}} + a c_{\mathrm{V}} \partial_\nu T_{\mu\nu}), \qquad (18)$$

where m_{q} denotes the bare subtracted quark mass, b_{V} and c_{V} are improvement coefficients, and $T^{\mu\nu}(x) = -\bar{\psi}(x)\frac{1}{2}[\gamma_\mu, \gamma_\nu]\tau^3\psi(x)$ is the tensor density. We used the nonperturbative estimate for the renormalization factor Z_{V} in the two-flavor theory of Refs. [40,41]. On the other hand, the conserved vector current, while not subject to renormalization, requires $\mathcal{O}(a)$ improvement even at tree level. In this work, we neither used the improved version of the point-split vector current, nor did we compute matrix elements containing the derivative of the tensor current. Therefore, our results for form factors and charge radii are not fully $\mathcal{O}(a)$ improved; hence, neglecting the b_{V} term in Eq. (18) is consistent.

In the remainder of this paper, we concentrate on results obtained using the conserved (point-split) vector current. We have checked explicitly that the local vector current yields fully consistent results, provided that it is properly renormalized. As a further check, we have estimated the renormalization factor Z_{V} on each ensemble from the ratio of matrix elements of the local and conserved current. We find agreement with the determination of Z_{V} at the respective β-value in the chiral limit [40] at the level of 1% or better.

The interpolating field for the proton was chosen as

$$\Psi^\alpha(x) = \epsilon_{abc}(u_a^T(x) C\gamma_5 d_b(x)) u_c^\alpha(x), \qquad (19)$$

with Gaussian-smeared quark fields [42]

$$\tilde{\psi} = (1 + \kappa_{\mathrm{G}}\Delta)^N \psi, \qquad (20)$$

where the links in the three-dimensional covariant Laplacian Δ were APE smeared [43] in the spatial directions to further enhance the projection properties onto the ground state and help reduce the gauge noise. Correlation functions were constructed using identically smeared interpolating fields at both the source and sink to ensure that the two-point functions are given by a sum of exponentials $e^{-E_n t}$ with positive coefficients. The smearing parameter κ_{G} and the iteration number N were tuned so as to maximize the length of the effective mass plateaux in a variety of channels. A widely used measure for the spatial extent of a smeared source vector is the "smearing radius" r_{sm} (for a definition, see, e.g., Eq. (2.6) in Ref. [44]). We note that our choice of κ_{G} and N corresponds to $r_{\mathrm{sm}} \approx 0.5$ fm. As was first noted in Ref. [44], the standard Gaussian smearing procedure becomes rapidly ineffective for baryons as the lattice spacing is decreased. Alternatively one may employ "free-form smearing" [44] which, however, cannot be readily applied at the sink. Therefore, all results presented in this paper have been obtained using standard Gaussian smearing at both the source and sink. Note that we did not employ boosted Gaussian smearing [45] either, because the boost is small for the nucleon, and the gain in terms of an enhanced projection on the ground state is expected to be marginal.

Smearing the quark fields in the spatial directions only, while required in order to keep the transfer matrix formalism intact, breaks the relativistic covariance of the interpolating fields constructed from smeared quarks. This issue has not been studied previously in any great detail in the context of nucleon form factors. In Appendix A, we give a brief explanation why the relativistic invariance of our results is not affected.

To compute the three-point function, we use the "fixed-sink" method, which requires an additional inversion for each value of t_s but allows both the operator insertion and

the momentum transfer to be varied without additional inversions [46]. To realize a range of values for the squared four-momentum transfer Q^2, we have computed the two- and three-point correlation functions for several spatial momenta $\boldsymbol{q} \equiv \boldsymbol{n}2\pi/L$, with $|\boldsymbol{n}|^2 = 0, 1, 2, \ldots, 6$.

The ratios R_{V_μ} of Eq. (13) contain a particular combination of nucleon two-point functions, in order to isolate the relevant matrix element. In our analysis, the two-point functions which enter R_{V_μ} were represented by single exponential fits. For nonvanishing momenta $\boldsymbol{q}$, the nucleon energies were determined from the nucleon mass using the continuum dispersion relation. We found that this procedure produced smaller statistical errors, in particular at higher values of the momentum transfer $\boldsymbol{q}^2$. It was checked explicitly that the direct determination of the energies in the nucleon channel from the exponential falloff of $C_2(\boldsymbol{q}, t)$ produced fully consistent results within statistical errors.

To express dimensionful quantities in physical units, we determined the lattice spacing for all our ensembles using the mass of the Ω baryon, as described in Ref. [47]. More recently, the ALPHA Collaboration has published accurate values for the lattice spacing determined from the kaon decay constant, f_K [48,49]. While the central values differ slightly, both determinations are well compatible within the quoted uncertainties. We have verified that uncertainties in the scale-setting procedure have no significant influence on the values of the charge radii in physical units.

C. Statistics and error analysis

We computed two- and three-point correlation functions on all ensembles listed in Table I. To increase statistics, we used multiple sources spread evenly across the lattice on each gauge configuration. The total number of measurements for each ensemble is listed in Table I. Statistical errors were estimated using a bootstrap procedure with 10,000 bootstrap samples. Note that we averaged measurements taken at different source positions on a given configuration prior to computing bootstrap samples.

Simulations at the fine lattice spacings considered here are known to be affected by the critical slowing down of the smooth modes of the gauge field and the freezing of the topological charge [50], leading to potentially long autocorrelation times. Ignoring the long tails in the autocorrelation function may lead to a significant underestimation of statistical errors [51]. Since the correlation functions of the nucleon studied here are intrinsically very noisy, however, one may expect that the contributions from the tails have relatively little influence on the overall statistical error.

We have investigated the impact of autocorrelations on our results by performing a binning analysis prior to applying the bootstrap procedure. To this end, we focused on the N6 ensemble, which is based on a long Monte Carlo sequence, comprising 8040 molecular dynamics units in total. Our findings indicate only a marginal increase in the statistical error of the electric form factor and the nucleon mass, which amounts to 2% at most. We conclude that, for the purpose of computing nucleon hadronic matrix elements and masses, our ensembles are sufficiently decorrelated.

III. EXCITED-STATE SYSTEMATICS

The standard "plateau method" for extracting G_{E} and G_{M} proceeds by fitting the ratios defined in Eq. (13) to a constant in the region where they are approximately independent of t and t_s, assuming that their asymptotic behavior has been reached. For the following discussion, it is useful to define an "effective" electric form factor, $G_{\mathrm{E}}^{\mathrm{eff}}(Q^2, t, t_s)$, by dividing out the kinematical factor in Eq. (14), i.e.,

$$G_{\mathrm{E}}^{\mathrm{eff}}(Q^2, t, t_s) = \sqrt{\frac{2E_{\boldsymbol{q}}}{m_N + E_{\boldsymbol{q}}}} R_{V_0}(\boldsymbol{q}, t, t_s). \tag{21}$$

A similar relation is used to define $G_{\mathrm{M}}^{\mathrm{eff}}(Q^2, t, t_s)$. As $t, (t_s - t) \to \infty$, the effective form factors will approach their asymptotic values with exponentially small corrections,

$$G_{\mathrm{E,M}}^{\mathrm{eff}}(Q^2, t, t_s) = G_{\mathrm{E,M}}(Q^2) + \mathcal{O}(e^{-\Delta t}) + \mathcal{O}(e^{-\Delta'(t_s - t)}), \tag{22}$$

where Δ and Δ' denote the energy gaps between the ground and first excited states for the initial- and final-state nucleons, respectively. Here, we omit the superscript "bare" on the form factors, since we assume that the ratios R_{V_μ} have been appropriately renormalized.

It is well known that nucleon correlation functions suffer from an exponentially increasing noise-to-signal ratio [52,53], which imposes a limit on the source-sink separation t_s which can be realized with reasonable numerical effort. In typical calculations, $t_s \approx 1.1$–1.2 fm, while separations as large as 1.4 fm have been reported only in very few cases [22,23]. Hence, to guarantee a reliable determination of G_{E} and G_{M} using the plateau method, the contributions from excited states in Eq. (22) must already be sufficiently suppressed for $t, (t_s - t) \lesssim 0.5$ fm. Moreover, since the gaps Δ and Δ' are proportional to m_π in the chiral regime, one expects that this effect will become even more pronounced for the more chiral ensembles.

In Fig. 2, we show effective mass plots for a nucleon at rest, computed at two different values of the lattice spacing at nearly fixed pion mass. One clearly sees that the ground state is isolated only for separations larger than 0.5 fm. Since the asymptotic behavior must be reached for both the initial- and final-state nucleons, which may also carry momentum, source-sink separations of the order of 1–1.5 fm seem rather small. Therefore, one cannot rule out a systematic bias, unless source-sink separations significantly larger than 1 fm are realized.

To minimize or eliminate such a bias in our final results, we employ three different methods:

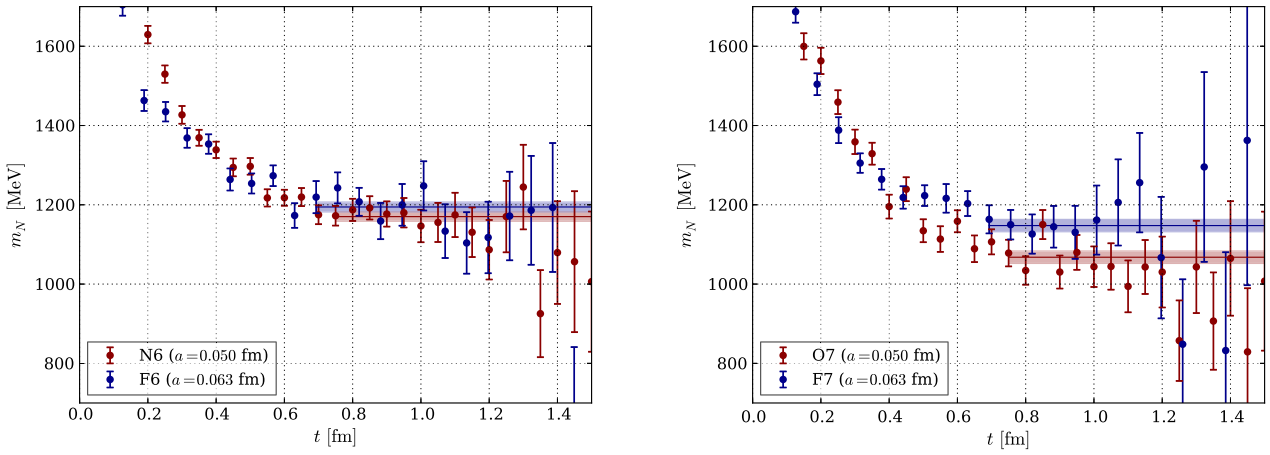

FIG. 2 (color online). Effective masses in the nucleon channel computed at two different lattice spacings for $m_\pi \approx 330$ MeV (left panel) and $m_\pi \approx 275$ MeV (right panel).

(i) *Plateau fits.*—For a fixed value of t_s, the quantities $G^{\mathrm{eff}}_{\mathrm{E,M}}(Q^2, t, t_s)$ are fitted to a constant over a small interval in t. The default value of the source-sink separation is $t_s \approx 1.1$ fm. For the high-statistics run on the N6-ensemble, we have also considered separations as large as $t_s = 1.4$ fm.

(ii) *Two-state fits.*—In this case, the leading contributions from excited states are included explicitly by using an *ansatz* of the form

$$G^{\mathrm{eff}}_{\mathrm{E,M}}(Q^2, t, t_s) = G_{\mathrm{E,M}}(Q^2) + c^{(1)}_{\mathrm{E,M}}(Q^2) e^{-\Delta t} + c^{(2)}_{\mathrm{E,M}}(Q^2) e^{-\Delta'(t_s - t)}, \tag{23}$$

with simultaneous fits in t and $t_s - t$ performed to the data collected for several source-sink separations t_s. To stabilize the fits and reduce the number of fit parameters, we fix the gaps to $\Delta = m_\pi$ and $\Delta' = 2m_\pi$, assuming that the lowest-lying excitations are described by multiparticle states, consisting of a nucleon and at least one pion. In our chosen kinematics. the nucleon at t_s is at rest, such that the lowest-lying multiparticle state consists of one nucleon and two pions in an S-wave. By contrast, the initial state carries momentum and, in the absence of πN interactions, therefore consists of a moving nucleon and a pion at rest, hence the choice $\Delta = m_\pi$. With these assumptions, we may determine the form factors $G_{\mathrm{E,M}}$ as well as the coefficients $c^{(1)}_{\mathrm{E,M}}$ and $c^{(2)}_{\mathrm{E,M}}$ as fit parameters for a given Q^2-value.[2]

(iii) *Summed insertions ("summation method").*—Following Refs. [24–26,54] and our previous work [22,27,55], we define the quantities $S_{\mathrm{E,M}}(Q^2, t_s)$ by

$$S_{\mathrm{E,M}}(Q^2, t_s) := a \sum_{t=a}^{t_s - a} G^{\mathrm{eff}}_{\mathrm{E,M}}(Q^2, t, t_s), \tag{24}$$

the asymptotic behavior of which is given by

$$S_{\mathrm{E,M}}(Q^2, t_s) \overset{t_s \gg 0}{\longrightarrow} K_{\mathrm{E,M}}(Q^2) + t_s G_{\mathrm{E,M}}(Q^2) + \ldots, \tag{25}$$

where $K_{\mathrm{E,M}}(Q^2)$ denote (in general divergent) constants and the ellipses stand for exponentially suppressed corrections. The precise form of the latter depends on the details of the spectrum. If, for instance, $\Delta = m_\pi$ and $\Delta' = 2m_\pi$, the leading correction is of the order $\exp\{-\Delta t_s\}$, while for $\Delta = \Delta'$, it is of the generic form

$$(A_{\mathrm{E,M}} + B_{\mathrm{E,M}} t_s) \exp\{-\Delta t_s\}, \tag{26}$$

with coefficients $A_{\mathrm{E,M}}$ and $B_{\mathrm{E,M}}$. By computing $S_{\mathrm{E,M}}(t_s)$ for several sufficiently large values of t_s, form factors can be determined from the slope of a linear fit. Since t_s is, by design, larger than either t or $(t_s - t)$, excited-state contributions are parametrically reduced compared to the plateau method. The summation method has been successfully applied in our earlier calculation of the nucleon axial charge [27] and also in recent studies of various nucleon matrix elements [23,56].

As a common feature among lattice calculations, we note that nucleon electromagnetic form factors are typically overestimated at a given value of Q^2 relative to the phenomenological representation of the experimental data [57], even when the calculation is performed for small pion masses. The three methods which we employ to determine $G_{\mathrm{E,M}}(Q^2)$ are compared in Fig. 3. Our data computed for different source-sink separations t_s show a systematic

[2]We have also performed two-state fits in which the gaps were left as fit parameters. The resulting estimates for the form factors were fully consistent but had much larger statistical errors.

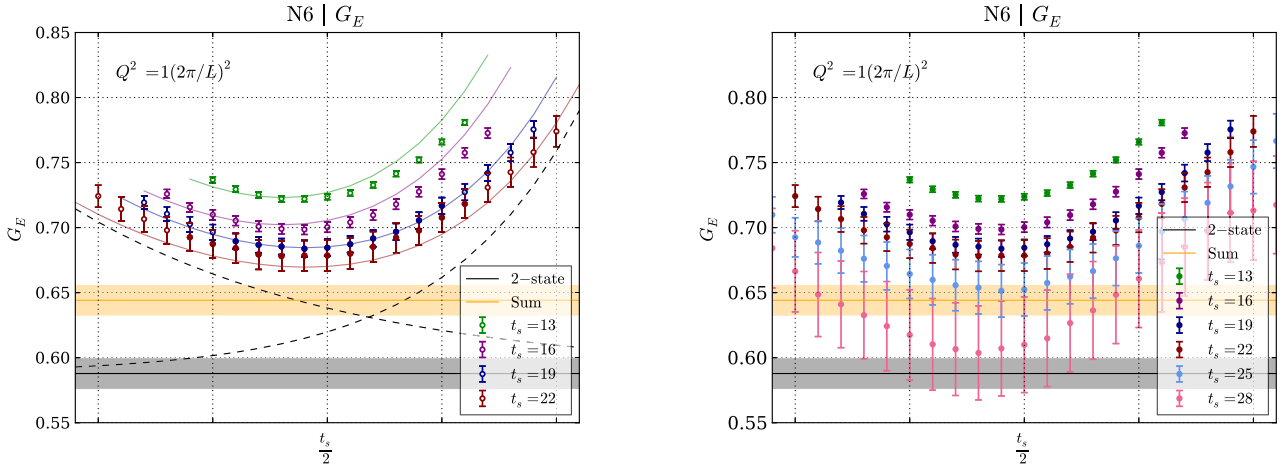

FIG. 3 (color online). Data for $G_{\mathrm{E}}^{\mathrm{eff}}$ computed for several values of t_s at the lowest nonzero momentum transfer on the N6 ensemble. The yellow band shows the result for G_{E} determined from the summation method. The solid curves are a representation of the data at individual values of t_s, as determined from a simultaneous two-state fit to the solid points in the left panel. The gray band denotes the corresponding asymptotic value. For the explanation of the dashed curves, see the text. The fits which correspond to the yellow and gray bands in both panels have been performed for $t_s \leq 1.1$ fm, i.e., $t_s/a \leq 22$.

downward trend as t_s is increased from 0.65 to 1.1 fm. This reinforces our concern that $t_s \approx 1.1$ fm is insufficient to rule out a systematic bias when the plateau method is applied. In comparison, the slope determined from the summed ratio in Eq. (25) yields a result for $G_{\mathrm{E}}(Q^2)$ which lies sufficiently below $G_{\mathrm{E}}^{\mathrm{eff}}(Q^2, t, t_s)$ for all t, t_s.

The result from the two-state fit is even smaller: The asymptotic value of $G_{\mathrm{E}}^{\mathrm{eff}}(Q^2, t, t_s)$ for $t, (t_s - t) \to \infty$ is represented by the gray band, while the dashed curves correspond to $G_{\mathrm{E}} + c_{\mathrm{E}}^{(1)} e^{-m_\pi t}$ and $G_{\mathrm{E}} + c_{\mathrm{E}}^{(2)} e^{-2m_\pi (t_s - t)}$, where G_{E}, $c_{\mathrm{E}}^{(1)}$, and $c_{\mathrm{E}}^{(2)}$ are determined from the fit. At face value, the sizeable gap between the result from the two-state fit and the data for $G_{\mathrm{E}}^{\mathrm{eff}}$ suggest that the latter are far from the asymptotic behavior when $t_s \leq 1.1$ fm. In particular, there is no overlap between the gray band and any of the data points from which it is determined. The dashed lines in the plot suggest that the two-state fit constrains G_{E} merely from the curvature in t at a given t_s and from the trend in the source-sink separation as the latter is increased. To investigate this further, we have added two more values of t_s to the N6 ensemble, corresponding to separations of 1.3 and 1.4 fm, respectively. The additional data for $G_{\mathrm{E}}^{\mathrm{eff}}$ are shown in the right panel of Fig. 3. In spite of the large statistical error, it is clear that $G_{\mathrm{E}}^{\mathrm{eff}}$ approaches the asymptotic value extracted from the two-state fit. We conclude that two-state fits applied to our data collected for $t_s \leq 1.1$ fm should not simply be discarded, even though the fit corresponding to the gray band in the left panel of Fig. 3 does not appear very convincing. We will thus include such results in our subsequent analysis but interpret them with the necessary amount of caution. Consequently, our preferred method for determining form factors remains the summation method.

IV. Q^2-DEPENDENCE AND CHIRAL BEHAVIOR

In this section, we discuss the dependence of form factors on the squared momentum transfer, Q^2, and their behavior as the pion mass is tuned toward its physical value. Here, we focus on the more qualitative features and defer a detailed discussion of chiral extrapolations based on baryonic ChPT to Sec. V.

A full set of results for $G_{\mathrm{E}}(Q^2)$ and $G_{\mathrm{M}}(Q^2)$ obtained from all three methods (i.e., plateau fits, summation method, and two-state fits) is presented in Tables VI–XVI in Appendix B. To describe the dependence on Q^2, we follow the standard procedure of fitting the results for $G_{\mathrm{E,M}}$ using a dipole ansatz motivated by vector meson dominance, i.e.,

$$G_{\mathrm{E}}(Q^2) = \left(1 + \frac{Q^2}{M_{\mathrm{E}}^2}\right)^{-2},$$
$$G_{\mathrm{M}}(Q^2) = G_{\mathrm{M}}(0) \cdot \left(1 + \frac{Q^2}{M_{\mathrm{M}}^2}\right)^{-2}. \quad (27)$$

Using the definition in Eq. (8), the charge radii are then obtained from

$$\langle r_{\mathrm{E,M}}^2 \rangle = \frac{12}{M_{\mathrm{E,M}}^2}. \quad (28)$$

The ratio $G_{\mathrm{M}}(Q^2)/G_{\mathrm{E}}(Q^2)$ is related to the nucleon's magnetic moment μ via

$$\mu \equiv 1 + \kappa = \left.\frac{G_{\mathrm{M}}(Q^2)}{G_{\mathrm{E}}(Q^2)}\right|_{Q^2=0}, \quad (29)$$

where κ denotes the anomalous magnetic moment. The reciprocal ratio $G_{\mathrm{E}}(Q^2)/G_{\mathrm{M}}(Q^2)$ is an interesting quantity

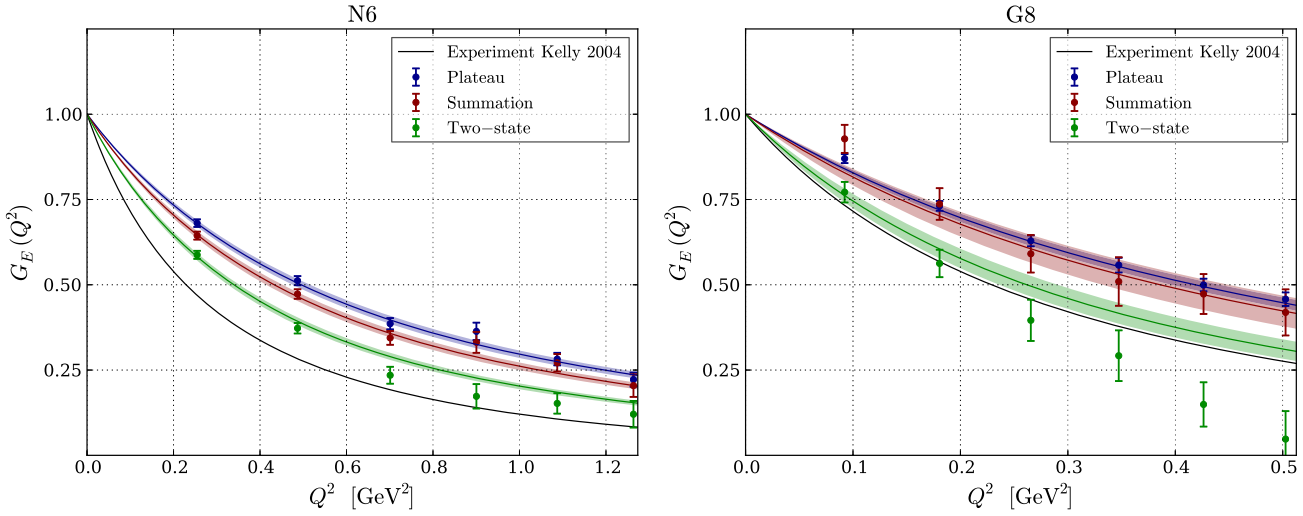

FIG. 4 (color online). Dipole fits of the Q^2-dependence of G_{E}, as determined using the plateau method (shown in blue), summed insertions (red), and two-state fits (green). The left and right panels correspond to pion masses of 331 and 193 MeV, respectively. The black line denotes Kelly's parametrization of experimental data.

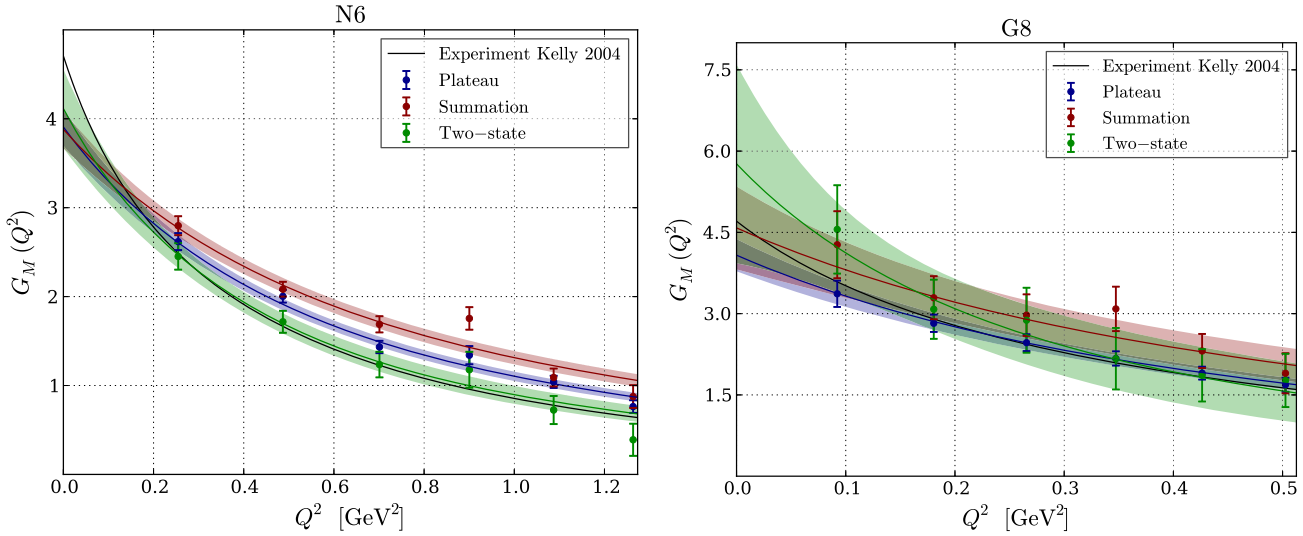

FIG. 5 (color online). Dipole fits of the Q^2-dependence of G_{M}. The meaning of the symbols is identical to Fig. 4.

regarding the discrepancy between experimental determinations based on Rosenbluth separation and the recoil polarization technique.

Examples of dipole fits to the form factor data obtained for two different pion masses are shown in Figs. 4 and 5, where they are compared to Kelly's phenomenological parametrization [57] of experimental data.[3] In comparing experimental and lattice results, one must bear in mind that the latter have been obtained at unphysical values of the pion mass.

Clearly, the slope of the electric form factor near $Q^2 = 0$ varies depending on the method which is used to determine G_{E} from the ratio of correlators. One observes that two-state fits produce by far the steepest dropoff, while the standard plateau method yields the flattest behavior in Q^2. This translates into a corresponding hierarchy for estimates of the electric charge radius, which are tabulated in Table II. As the pion mass is lowered toward its physical value, one also finds that the spread in the results for $\langle r_{\mathrm{E}}^2 \rangle$ becomes more pronounced among the three methods. This is consistent with the assertion that the issue of unsuppressed excited-state contributions becomes increasingly important near the physical pion mass.

[3]We employ Kelly's parametrization as a benchmark, since the differences between Kelly's and the more recent parametrization by Arrington and Sick [58], as well as the dispersive analysis by Lorenz *et al.* [59] are too small to be resolved at the level of statistical precision provided by our data.

TABLE II. Electric and magnetic charge radii and magnetic moment as determined from the three methods on each of our ensembles.

Run	Method	$\langle r_E^2 \rangle$ (fm^2)	$\langle r_M^2 \rangle$ (fm^2)	μ
A3	Plat	0.310(14)	0.355(29)	4.22(17)
	Sum	0.335(27)	0.391(56)	4.65(34)
	Two-state	0.339(18)	0.425(55)	4.48(29)
A4	Plat	0.362(23)	0.324(52)	3.65(29)
	Sum	0.462(55)	0.190(63)	3.15(38)
	Two-state	0.453(35)	0.216(71)	3.42(43)
A5	Plat	0.413(26)	0.395(59)	3.69(31)
	Sum	0.504(57)	0.333(98)	3.72(51)
	Two-state	0.543(56)	0.53(21)	4.3(1.0)
B6	Plat	0.427(22)	0.442(32)	3.89(17)
	Sum	0.581(89)	0.42(10)	4.11(49)
	Two-state	0.585(56)	0.69(18)	4.90(62)
E5	Plat	0.304(14)	0.318(44)	4.03(30)
	Sum	0.336(22)	0.373(69)	4.21(45)
	Two-state	0.385(19)	0.367(69)	4.16(48)
F6	Plat	0.407(17)	0.387(27)	3.67(18)
	Sum	0.451(23)	0.502(49)	4.15(25)
	Two-state	0.505(21)	0.366(68)	3.32(33)
F7	Plat	0.421(25)	0.385(45)	3.72(25)
	Sum	0.431(29)	0.446(62)	4.17(31)
	Two-state	0.518(35)	0.54(24)	3.57(80)
G8	Plat	0.463(25)	0.505(58)	4.08(30)
	Sum	0.502(76)	0.45(13)	4.58(73)
	Two-state	0.739(76)	0.85(39)	5.8(1.6)
N5	Plat	0.333(12)	0.314(24)	3.85(16)
	Sum	0.383(29)	0.361(60)	3.93(35)
	Two-state	0.381(12)	0.399(34)	4.18(21)
N6	Plat	0.391(16)	0.412(33)	3.91(21)
	Sum	0.448(19)	0.336(33)	3.88(21)
	Two-state	0.571(22)	0.535(91)	4.11(43)
O7	Plat	0.396(19)	0.399(37)	3.45(19)
	Sum	0.460(23)	0.436(42)	3.66(21)
	Two-state	0.672(38)	0.99(20)	4.98(69)

For G_M, the systematic trend in the Q^2-dependence is not so clearly visible as in the case of the electric form factor and charge radius, which is partly due to the larger statistical errors. Qualitatively, one observes that our lattice data for $G_M(Q^2)$ show better overall agreement with the representation of the experimental data, regardless of the method which with the former have been obtained.

Dipole fits to the data for $G_M(Q^2)$ extracted from two-state fits show a slight—albeit statistically insignificant—tendency for larger intercepts at vanishing Q^2, resulting in somewhat higher estimates for the magnetic moment, μ. Moreover, these fits reveal that the electric and magnetic radii turn out to be rather similar (see Table II). The fact that G_M/G_E shows no statistically significant deviation from a constant within the Q^2-range we are able to investigate (see Fig. 6) is consistent with the experimental data extracted using the traditional Rosenbluth separation technique.

To further assess the effectiveness of the three methods employed to extract the form factors, we have studied their chiral behavior at a reference value of the four-momentum transfer of $Q^2_{\text{ref}} = 0.1$ GeV^2. This is very close to the smallest nonzero value of Q^2 on the G8 ensemble, i.e., at our smallest pion mass. Using the dipole fit parameters, we have obtained $G_E(Q^2_{\text{ref}})$ and $G_M(Q^2_{\text{ref}})$ for all ensembles in our set. Similarly, we employed the phenomenological parametrization to produce the corresponding estimates from experiment at Q^2_{ref} and at the physical pion mass. The results are shown in Fig. 7. The plateau method clearly overestimates G_E, as there is no observable tendency for the data at different pion masses to approach the experimental result. The summation performs slightly better but does not improve the situation substantially. Only the data based on two-state fits show a trend which brings them into agreement with experiment at the physical pion mass. For the magnetic form factor, the situation is more favorable: The plateau method only slightly underestimates G_M relative to

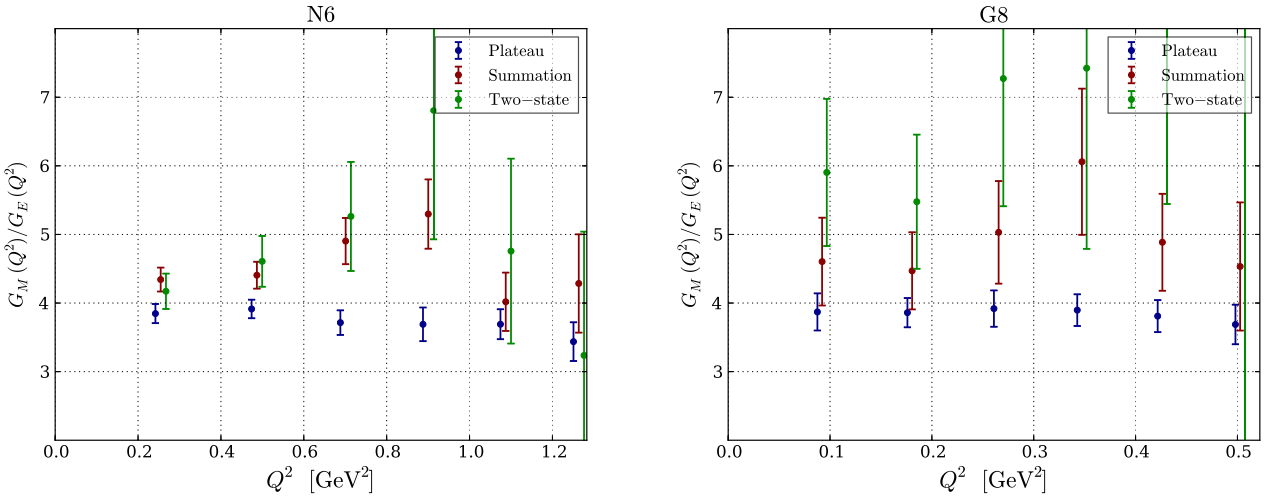

FIG. 6 (color online). The Q^2-dependence of G_M/G_E.

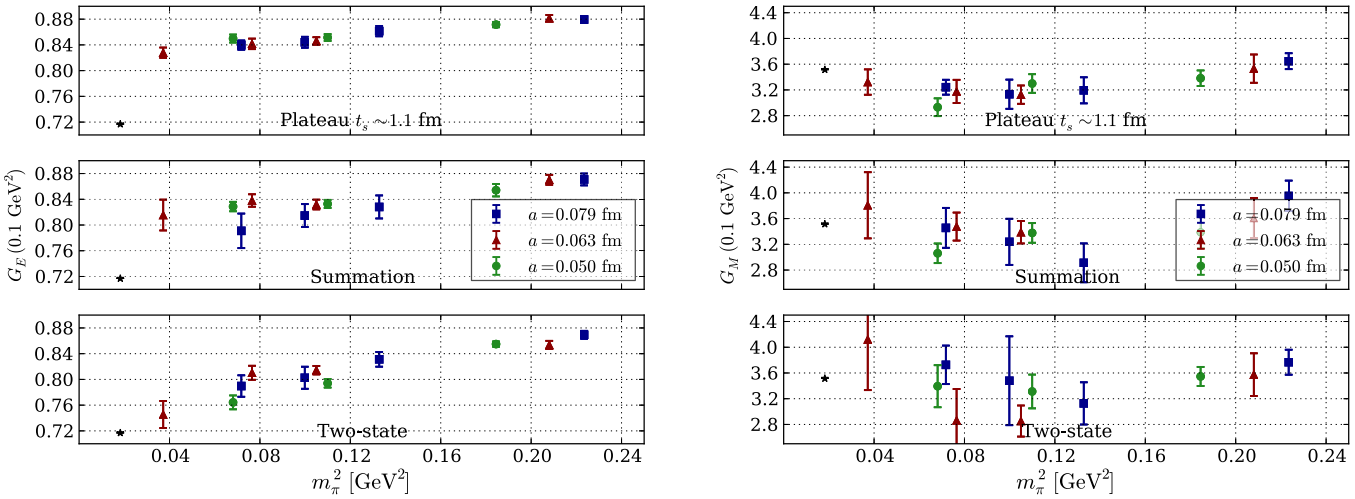

FIG. 7 (color online). Comparison of the three methods for extracting the nucleon form factors G_E (left) and G_M (right) at a fixed value of Q^2. Shown are, from top to bottom, the results from the plateau method, summation method, and two-state fit, as a function of m_π^2.

the experiment, while the chiral trend in the data extracted using the summation method or two-state fits agrees well with Kelly's parametrization.

We conclude that the summation method cannot fully reconcile lattice data for G_E with its phenomenological value. Such an agreement can only be reached if one is willing to trust two-state fits.

V. CHIRAL FITS

Our task is now to make contact between lattice data for form factors obtained for a range of pion masses and lattice spacings and the quantities which describe key properties of the nucleon, namely the charge radii and the magnetic moments. This link is provided by the chiral effective field theory. The approach which has so far been most widely applied to perform chiral extrapolations of lattice results for these quantities is based on heavy baryon chiral perturbation theory (HBChPT) [60], supplemented by the inclusion of the Δ-resonance [61,62].

Here, we employ an alternative formalism, i.e., the manifestly Lorentz-invariant version of baryonic ChPT [29–31], which has also been extended to include the Δ-resonance [63], as well as vector mesons [32,64]. Our procedure resembles the strategy pursued in Ref. [32] to extract charge radii and magnetic moments from experimental data of nucleon form factors. In particular, we focus on fitting the dependence of the form factors G_E and G_M on the pion mass and the squared momentum transfer Q^2 to the expressions of baryonic effective field theory (EFT), including vector degrees of freedom. The relevant EFT expressions for G_E and G_M have been supplemented by terms which describe the dependence on the lattice spacing a. In this way, we combine a simultaneous chiral and continuum extrapolation with a fit to the Q^2-dependence of form factors. To enable a comparison with the standard approach, we also perform fits to the pion mass dependence of charge radii and the magnetic moment to several variants of HBChPT.

Specifically, we consider the manifestly Lorentz-invariant effective Lagrangian describing πN interactions including vector mesons at $\mathcal{O}(q^3)$ in the chiral expansion. A detailed discussion of this effective Lagrangian can be found in Ref. [32]. Table III gives an overview of the various interaction terms, as well as the associated low-energy constants and hadron masses. From the table, one can read off which low-energy constants are determined by our fitting procedure and which phenomenological information is used to fix the values of the remaining ones. We note that the interaction terms proportional to c_7 and d_7 do not contribute in the isovector case considered here. We have also dropped the contributions from the ω-meson entirely, since they were found to have only a negligible effect on the results [32]. Furthermore, in Ref. [65], it was shown that the universal ρ-meson coupling constant g can be fixed via the Kawarabayashi–Suzuki–Riadzuddin–Fayyazuddin (KSRF) relation [66,67], which follows by requiring the self-consistency of an effective chiral theory involving a pion, nucleons, and the ρ-meson.

The full expressions for the chiral expansions of the Dirac and Pauli form factors to $\mathcal{O}(q^3)$ are given in Appendix D.2 of Ref. [68] but are too lengthy to be displayed here. Starting from those formulas, we have formed the appropriate linear combinations for the isovector form factors G_E and G_M. The resulting expressions were used to perform a simultaneous fit to both $G_E(Q^2)$ and $G_M(Q^2)$ obtained for a range of pion masses and momentum transfers, at all three values of the lattice spacing.[4] Cutoff effects can be easily incorporated

[4]To evaluate the loop integrals appearing in the expressions, we make use of LoopTools [69,70].

TABLE III. Interaction terms of the chiral effective theory used for fitting lattice data for nucleon electromagnetic form factors. A circle on top of a symbol indicates that the corresponding low-energy parameter is defined in the chiral limit. The third column describes how their values are determined. Further details are described in the text.

Interaction	Low-energy parameter	Value
$\mathcal{L}^{(2)}$	F	$F_\pi^{\rm exp} = 92.2$ MeV
	M_π^2	Lattice input
$\mathcal{L}_{\rho,\rm eff}$	$\mathring{m}_\rho$	$m_\rho^{\rm exp} = 775$ MeV or lattice input
	g	$g = m_\rho/\sqrt{2}F_\pi = 5.93$ from KSRF relation
$\mathcal{L}_{\pi\rho}$	d_x	Fit parameter
$\mathcal{L}_{\pi\rho N}$	g	From KSRF relation
	G_ρ	Fit parameter
$\mathcal{L}^{(1)}_{\pi N}$	$\mathring{m}_{\rm N}$	$m_{\rm N}^{\rm exp} = 938$ MeV or lattice input
	$\mathring{g}_{\rm A}$	$g_{\rm A}^{\rm exp} = 1.27$
$\mathcal{L}^{(2)}_{\pi N}$	c_6	Fit parameter
	c_7	c_7 does not contribute in the isovector case
$\mathcal{L}^{(3)}_{\pi N}$	d_6	Fit parameter
	d_7	d_7 does not contribute in the isovector case
$\mathcal{L}^{(1)}_{\pi\Delta}$	$\mathring{m}_\Delta$	$m_\Delta^{\rm exp} = 1210$ MeV
$\mathcal{L}^{(1)}_{\pi N\Delta}$	$g_{\pi N\Delta}$	1.125, from fit to $\Delta \to \pi N$ decay width

into this framework by adding terms proportional to the lattice spacing a to the form factors, i.e.,

$$G_{\rm E}(Q^2) = G_{\rm E}^{\rm EFT}(Q^2) + aQ^2\beta_{\rm E},$$
$$G_{\rm M}(Q^2) = G_{\rm M}^{\rm EFT}(Q^2) + a\beta_{\rm M}, \tag{30}$$

where $G_{\rm E,M}^{\rm EFT}$ denote the continuum EFT expressions for the form factors, while the coefficients $\beta_{\rm E,M}$ are taken as fit parameters. This ansatz takes account of the fact that the matrix element corresponding to the electric form factor is $\mathcal{O}(a)$ improved at vanishing momentum transfer.

Estimates for the charge radii $\langle r_{\rm E}^2\rangle$, $\langle r_{\rm M}^2\rangle$ and the anomalous magnetic moment κ are obtained by inserting the fitted values of the low-energy parameters of d_x, G_ρ, d_6, and $\tilde{c}_6 \equiv c_6 - G_\rho/2g$ into the corresponding EFT expressions, i.e.,

$$\langle r_{\rm E,M}^2\rangle = -\frac{6}{G_{\rm E,M}(0)}\frac{dG_{\rm E,M}(Q^2)}{dQ^2}\bigg|_{Q^2=0}, \tag{31}$$

$$\kappa = G_{\rm M}(0) - 1. \tag{32}$$

The relations between these quantities and the Dirac radius $\langle r_1^2\rangle$, as well as the combination $\kappa\langle r_2^2\rangle$ reads

$$\langle r_1^2\rangle = \langle r_{\rm E}^2\rangle - \frac{6\kappa}{4m_{\rm N}^2},$$
$$\kappa\langle r_2^2\rangle = (1+\kappa)\langle r_{\rm M}^2\rangle - \langle r_{\rm E}^2\rangle + \frac{6\kappa}{4m_{\rm N}^2}. \tag{33}$$

We refer to a fit applied to form factor data obtained from the summation method, over the entire range of Q^2, with a pion mass cut of $m_\pi \le m_\pi^{\rm cut} = 330$ MeV, and the masses of the ρ-meson and nucleon fixed to their experimental values as our standard procedure. Standard fits were performed with and without terms parametrizing lattice artifacts [see Eq. (30)]. For the fit including lattice artifacts, one finds $\chi^2_{\rm red} = 1.21$, for 66 degrees of freedom. Results for the quantities $\langle r_{\rm E}^2\rangle$, $\langle r_{\rm M}^2\rangle$, κ, $\langle r_1^2\rangle$, and the combination $\kappa\langle r_2^2\rangle$ are listed in Table IV. One observes that fits with and without $\mathcal{O}(a)$ terms produce compatible results: Differences at the level of at most 1.5 standard deviations are seen in $\langle r_{\rm M}^2\rangle$ and κ. This indicates that the influence of lattice artifacts on the results is small.

A first qualitative assessment can be made by plotting the Q^2-dependence of $G_{\rm E}$ and $G_{\rm M}$ at the physical point compared to various phenomenological parametrizations of experimental data, as shown in Fig. 8. While the dependence of $G_{\rm E}$ on the squared momentum transfer is somewhat

TABLE IV. Results for charge radii and magnetic moments from direct fits to the form factors. Lines 3–7 contain the differences between variants of the fitting procedure as labelled in Table V and the results from the standard fit performed without $\mathcal{O}(a)$-terms. For instance, variant 5 yields $\langle r_{\rm E}^2\rangle = 0.831$.

$\langle r_{\rm E}^2\rangle$ (fm^2)	$\langle r_{\rm M}^2\rangle$ (fm^2)	κ	$\langle r_1^2\rangle$ (fm^2)	$\kappa\langle r_2^2\rangle$ (fm^2)	Fit
0.722(34)	0.720(53)	3.33(35)	0.501(41)	2.61(9)	Standard, with $\mathcal{O}(a)$-terms
0.748(12)	0.636(8)	3.93(11)	0.487(14)	2.65(9)	Standard, without $\mathcal{O}(a)$-terms
−0.013	−0.004	−0.15	−0.003	−0.11	Variant 1
+0.030	−0.025	+0.28	+0.011	+0.04	Variant 2
−0.001	−0.009	−0.14	+0.009	−0.14	Variant 3
+0.030	+0.035	−0.40	+0.057	−0.16	Variant 4
+0.083	+0.029	−0.16	+0.093	−0.05	Variant 5

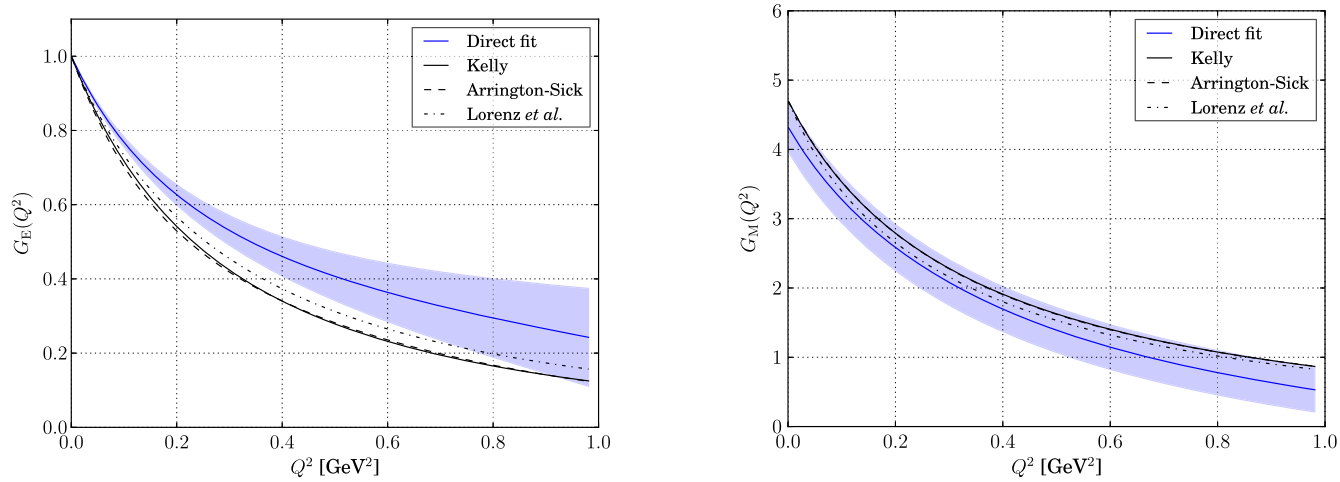

FIG. 8 (color online). The Q^2-dependence of G_E and G_M at the physical pion mass and in the continuum limit, as determined from a simultaneous fit to lattice data ("direct" fit) including lattice artifacts. The bands denote the statistical error. The solid, dashed, and dashed-dotted curves are the phenomenological representations of experimental data of Refs. [57], [58], and [59], respectively.

flatter compared to experiment, the behavior of G_M is reproduced very well.

To estimate the systematic error, we have considered a number of variations in the fitting procedure, which are compiled and labelled in Table V. These include different pion mass cuts, restrictions of the fitted range in Q^2, and the use of the masses of the ρ and nucleon determined by the lattice calculation at the respective value of the pion mass. These variations are indicative of higher-order terms in the chiral expansion and probe the overall consistency of our particular EFT approach. We have also estimated the residual systematic uncertainty due to excited states, by repeating the entire procedure using the form factor data obtained from two-state fits. Variations of the fitting procedure (corresponding to the entries in lines 3–7 in Table IV) were always applied neglecting terms parametrizing lattice artifacts (i.e., for $\beta_E = \beta_M = 0$), as this produced more stable fits, in particular when imposing more aggressive cuts in the pion mass or Q^2 range. However, while the systematic error budget is estimated from fits excluding lattice artifacts, we prefer to quote our main results using fits in which $\mathcal{O}(a)$-terms have been accounted for.

TABLE V. The standard procedure for fitting nucleon form factors to the expressions from baryonic ChPT and the variants applied in order to estimate the systematic error.

Standard fit	Variants	Label
Impose pion mass cut of $m_\pi^{\mathrm{cut}} \leq 330$ MeV	$m_\pi^{\mathrm{cut}} \leq 300$ MeV	1
	No mass cut	2
Fit entire available range in Q^2	Impose cut of $Q^2 < 0.5$ GeV^2	3
Use experimental values for m_N, m_ρ	Use lattice input for m_N, m_ρ	4
Fit data obtained using the summation method	Fit data extracted from two-state fits	5

We thus obtain as our final results:

$$\begin{aligned}
\langle r_E^2 \rangle &= 0.722 \pm 0.034(\mathrm{stat})^{+0.030}_{-0.013}(\chi\mathrm{fit})^{+0.083}_{-0.000}(\mathrm{exc})\ \mathrm{fm}^2,\\
\langle r_M^2 \rangle &= 0.720 \pm 0.053(\mathrm{stat})^{+0.035}_{-0.025}(\chi\mathrm{fit})^{+0.029}_{-0.000}(\mathrm{exc})\ \mathrm{fm}^2,\\
\kappa &= 3.33 \pm 0.35(\mathrm{stat})^{+0.28}_{-0.40}(\chi\mathrm{fit})^{+0.00}_{-0.16}(\mathrm{exc}),\\
\langle r_1^2 \rangle &= 0.501 \pm 0.041(\mathrm{stat})^{+0.057}_{-0.003}(\chi\mathrm{fit})^{+0.093}_{-0.000}(\mathrm{exc})\ \mathrm{fm}^2,\\
\kappa\langle r_2^2 \rangle &= 2.61 \pm 0.09(\mathrm{stat})^{+0.04}_{-0.16}(\chi\mathrm{fit})^{+0.00}_{-0.05}(\mathrm{exc})\ \mathrm{fm}^2.
\end{aligned} \tag{34}$$

Here, the systematic uncertainties estimated from fit variants 1–4 have been combined into an overall chiral fitting error, while the difference between employing the summation method and two-state fits is quoted as a separate, residual systematic uncertainty arising from excited states.

We did not consider fits to baryonic EFT including Δ degrees of freedom when assessing our systematic errors, as such fits produced unacceptably large values of χ^2_{red} when the low-energy parameter $g_{\pi N\Delta}$ was fixed to the phenomenological value of 1.125. On the other hand, treating $g_{\pi N\Delta}$ as a fit parameter resulted in an unphysically small value.

In Figs. 9 and 10, we compare the estimates for $\langle r_E^2 \rangle$, $\langle r_M^2 \rangle$, and κ at the physical point (shown as yellow points) with the experiment. While $\langle r_M^2 \rangle$ and κ agree quite well with the experimental results within statistical errors, we find that direct fits to the form factors underestimate the electric radius. However, given the large systematic uncertainty, we note that our estimate for $\langle r_E^2 \rangle$ is not incompatible

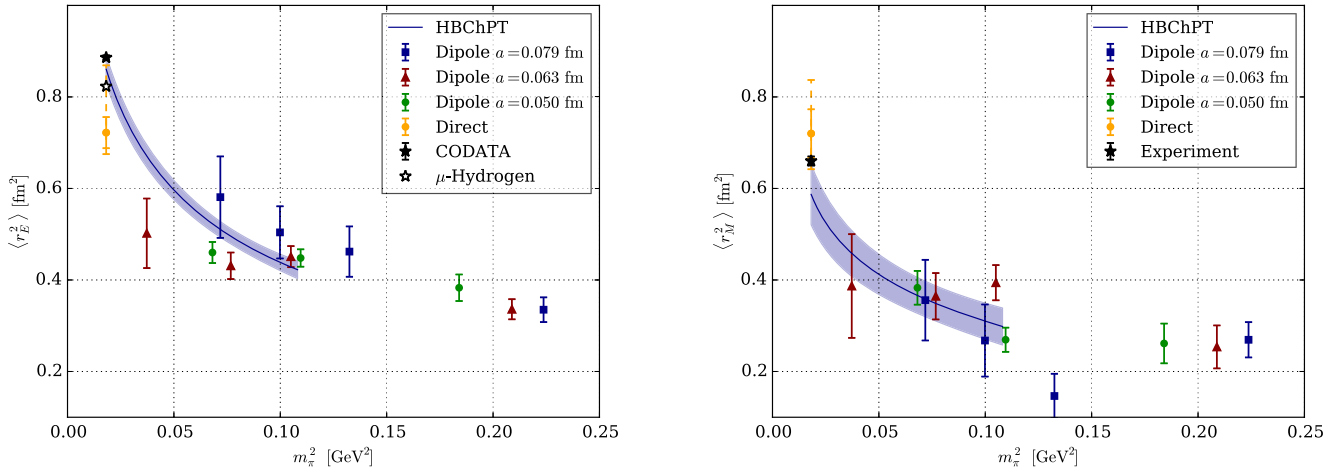

FIG. 9 (color online). Pion mass dependence of electric and magnetic radii extracted by fitting the Q^2-dependence of form factors to a dipole form. Chiral fits to HBChPT for $m_\pi \leq 330$ MeV and their statistical uncertainty are represented by the bands. The yellow points denote the results obtained by directly fitting the form factors to the EFT expressions. The associated systematic uncertainties are shown by the dashed error bars.

with either the CODATA result [10] or the value determined from muonic hydrogen [8,9].

To enable a comparison with previous lattice determinations [11–23], we have performed chiral extrapolations of our data to the expressions of HBChPT including the Δ-resonance at $\mathcal{O}(\epsilon^3)$ in the small scale expansion [61]. In particular, we fitted the pion mass dependence of our data for the Dirac radius $\langle r_1^2 \rangle$, the anomalous magnetic moment κ, and the combination $\kappa \langle r_2^2 \rangle$ to the expressions of Refs. [61,62,71], which are summarized, e.g., in Appendix A of Ref. [23]. In these fits, the low-energy parameters g_A, F_π, and $g_{\pi N \Delta}$ have been fixed to the same values as in Table III. An additional parameter, the photon-nucleon-Δ coupling, was fixed to the value −2.26 [71].

The results of such a HBChPT fit, with a pion mass cut of 330 MeV, without terms parametrizing cutoff effects and with the masses of the nucleon and Δ fixed to

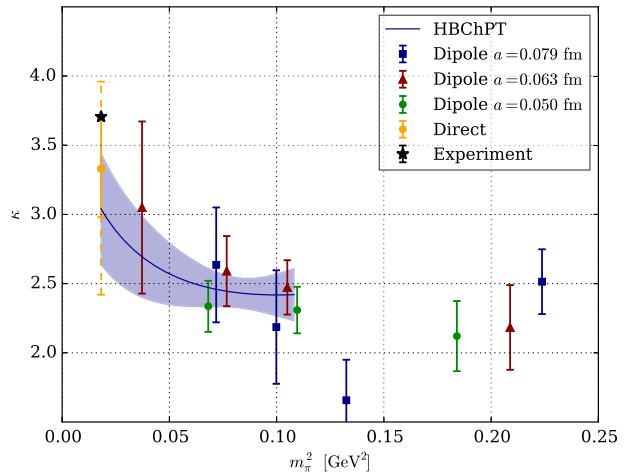

FIG. 10 (color online). Pion mass dependence of the anomalous magnetic moment. For an explanation of symbols, see Fig. 9.

$m_N = 938$ MeV and $m_\Delta = 1210$ MeV, respectively, are shown in Fig. 9. While the value for $\langle r_M^2 \rangle$ agrees within statistical errors with the result determined from directly fitting the form factors, there is a deviation by more than two standard deviations in the case of $\langle r_E^2 \rangle$, which, however, becomes insignificant when systematic errors are taken into account. Interestingly, the result for the electric radius obtained from the HBChPT fit is statistically compatible with both the CODATA estimate and the value determined from muonic hydrogen. However, a number of comments are in order. First, we note that HBChPT fits including terms parametrizing lattice artifacts mostly fail. This may be due to the lack of a clear trend in the data for the charge radii as the lattice spacing is varied. Second, fits based on HBChPT depend much more strongly on whether the input data originate from applying the summation method or two-state fits.

We note in passing that we have also applied baryonic EFT based on the Lagrangian described in Table III to perform chiral extrapolations of charge radii and κ as an alternative to HBChPT. The results at the physical point are consistent with direct fits to the form factors within statistical errors, except for the anomalous magnetic moment. We conclude that the chiral behavior of the quantities computed here is not fully understood in terms of baryonic chiral effective theory. To clarify the situation, it is mandatory to obtain more statistically precise data at the physical pion mass.

Given that the results for the charge radii and κ exhibit a large spread depending on the details of the chiral fitting procedure, the agreement of the HBChPT result for $\langle r_E^2 \rangle$ with the experimental values must be considered an accident. Due to the better overall stability, we prefer to quote our final estimates from fits applied directly to the form factors G_E and G_M [see Eq. (34)].

VI. CONCLUSIONS AND OUTLOOK

We have performed a comprehensive study of the isovector electromagnetic form factors of the nucleon in two-flavor QCD with a strong emphasis on controlling the various sources of systematic errors. Our findings culminate in the estimates shown in Eq. (34) for the charge radii and magnetic moment including a full error budget.

While the summation method provides a handle to explore excited-state contributions independently of the standard plateau method, the issue of a systematic bias could not be fully resolved. Although we prefer the summation method, since it does not rely on specific values of the energy gaps, two-state fits produce values that appear to reproduce the phenomenological situation better. However, for lack of data at source-sink separations of more than 1.5 fm, we cannot currently resolve the issue completely. Still, our data support the notion that agreement with experiment can be obtained by mapping out the pion mass dependence close to the physical point in conjunction with addressing the issue of excited-state contaminations, which has a greater impact as the pion mass is reduced.

Our study comprises three lattice spacings in the range 0.05–0.08 fm. In general, we find lattice artifacts to be small. This is most easily inferred from Figs. 9 and 10, which demonstrate that results for the charge radii and κ obtained on each ensemble show no significant difference as the lattice spacing is varied.

For the first time, we publish a complete error budget for baryonic charge radii and magnetic moments. Also for the first time, we have applied the method of Ref. [32], i.e., applying the full framework of covariant baryonic chiral effective theory to the nucleon electromagnetic form factors, in the context of lattice QCD.

While the wider picture of the convergence properties of the various forms of baryonic chiral effective theory cannot be fully addressed with our data, we have a clear preference for applying the fully covariant chiral effective theory to the form factors themselves. In particular, this avoids the systematic uncertainties inherent in the use of the somewhat simplistic dipole description of the form factors.

To further resolve the issue of excited-state effects, significant improvements in statistical precision at larger source-sink separations will be required. One proposed way to achieve this is the use of methods such as all-mode averaging [72] in order to reduce the associated computational costs. The first studies have yielded encouraging results, and we intend to pursue this avenue further. Another direction for improvement will be to make use of the variational method [54,73–75] for increased control and suppression of excited-state contributions.

Going beyond the isovector form factors to the proton and neutron form factors will require the inclusion of quark-disconnected diagrams, which makes it necessary to use all-to-all propagators. By employing stochastic estimators along with a generalized hopping parameter expansion, the scalar charge radius of the pion, which receives a significant contribution from quark-disconnected diagrams, has recently been measured on the lattice with an overall accuracy rivaling that of phenomenological determinations [76–78]. Related methods have been employed by other groups to study the nucleon structure quantities with disconnected parts [26,79–81], and we intend to further address the proton radius puzzle from the lattice side by using these and similar methods to separately study proton and neutron form factors in the future.

ACKNOWLEDGMENTS

The authors acknowledge the contributions of Andreas Jüttner to the early stages of this work. We thank Jeremy Green for useful discussions concerning the results of Refs. [23,56] and Eigo Shintani for discussions on all-mode averaging. We are grateful to our colleagues within the CLS initiative for sharing ensembles. These calculations were partly performed on the HPC Cluster "Wilson" at the Institute for Nuclear Physics, University of Mainz. We thank Christian Seiwerth for technical support. We are grateful for computer time allocated to project HMZ21 on the BG/Q "JUQUEEN" computer at NIC, Jülich. This work was granted access to the HPC resources of the Gauss Center for Supercomputing at Forschungzentrum Jülich, Germany, made available within the Distributed European Computing Initiative by the PRACE-2IP, receiving funding from the European Community's Seventh Framework Programme (FP7/2007-2013) under Grant No. RI-283493. This work was supported by the DFG through SFB 443 and SFB 1044 and by the Rhineland-Palatinate Research Initiative. M. D. M. was partially supported by the Danish National Research Foundation under Grant No. DNRF:90. T. R. was supported by DFG Grant No. HA4470/3-1. H. W. is grateful to the Yukawa Institute for Theoretical Physics, Kyoto University, for hospitality during the YITP workshop YITP-T-14-03 on "Hadrons and Hadron Interactions in QCD" where part of this work was completed. G. v. H. thanks the Tata Institute for Fundamental Research (Mumbai, India) for its hospitality during the workshop "Perspectives and Challenges in Lattice Gauge Theories," February 2015.

APPENDIX A: USE OF NONCOVARIANT INTERPOLATING OPERATORS IN NUCLEON FORM FACTOR CALCULATIONS

Typically, the interpolating nucleon operators used in lattice form factor calculations are not Lorentz covariant, due to the spatial smoothing procedures applied on the elementary fields. If we denote the overlap of the interpolating operator $\Psi_\alpha(x)$ onto the nucleon as[5]

[5]The states are normalized according to $\langle N, \boldsymbol{p}', s' | N, \boldsymbol{p}, s \rangle = 2E_{\boldsymbol{p}} \delta_{ss'} (2\pi)^3 \delta^{(3)}(\boldsymbol{p}' - \boldsymbol{p})$.

$$\langle 0|\Psi_\alpha(0,\boldsymbol{x})|N,\boldsymbol{p},s\rangle = U^s_\alpha(\boldsymbol{p})e^{i\boldsymbol{p}\cdot\boldsymbol{x}}, \tag{A1}$$

the question then poses itself, whether the fact that $U^s_\alpha(\boldsymbol{p})$ does not obey the Dirac equation affects the calculation in any way.

We denote by $u^s(\boldsymbol{p})$ the usual plane-wave solutions to the Dirac equation,[6] normalized according to

$$\bar{u}^r(\boldsymbol{p})u^s(\boldsymbol{p}) = 2m_N\delta^{rs} \tag{A2}$$

and obeying the spin sum rule

$$\sum_{s=1,2} u^s(\boldsymbol{p})\bar{u}^s(\boldsymbol{p}) = E_{\boldsymbol{p}}\gamma_0 - i\boldsymbol{p}\cdot\boldsymbol{\gamma} + m_N. \tag{A3}$$

Let $\psi_\alpha(x)$ be a nucleon interpolating field which does transform as a covariant Dirac spinor. Then its overlap onto the nucleon state has the form

$$\langle 0|\psi_\alpha(0,\boldsymbol{x})|N,\boldsymbol{p},s\rangle = Z_l u^s_\alpha(\boldsymbol{p})e^{i\boldsymbol{p}\cdot\boldsymbol{x}}, \tag{A4}$$

where Z_l is independent of $\boldsymbol{p}$ and can be chosen real and positive by an appropriate choice of the phase of the field $\psi_\alpha(x)$. To answer the question formulated above, we analyze the covariance properties of correlation functions of the operators $\Psi_\alpha(x)$ and $\psi_\alpha(x)$. We will focus on the asymptotic behavior of the correlation functions at large Euclidean time separations, where they are saturated by the nucleon ground state, and we indicate this by a $\star$ in the equations below.

We consider the following two-point functions and their spectral representation for $x_0 > 0$,

$$C^{\alpha\beta}_{2,ss}(\boldsymbol{p},x_0) \equiv \int d^3x e^{-i\boldsymbol{p}\cdot\boldsymbol{x}}\langle\Psi_\alpha(x)\bar{\Psi}_\beta(0)\rangle \stackrel{\star}{=} \frac{e^{-E_{\boldsymbol{p}}x_0}}{2E_{\boldsymbol{p}}}\sum_s U^s_\alpha(\boldsymbol{p})\bar{U}^s_\beta(\boldsymbol{p}), \tag{A5}$$

$$C^{\alpha\beta}_{2,sl}(\boldsymbol{p},x_0) \equiv \int d^3x e^{-i\boldsymbol{p}\cdot\boldsymbol{x}}\langle\Psi_\alpha(x)\bar{\psi}_\beta(0)\rangle \stackrel{\star}{=} Z^*_l\frac{e^{-E_{\boldsymbol{p}}x_0}}{2E_{\boldsymbol{p}}}\sum_s U^s_\alpha(\boldsymbol{p})\bar{u}^s_\beta(\boldsymbol{p}), \tag{A6}$$

$$C^{\alpha\beta}_{2,ls}(\boldsymbol{p},x_0) \equiv \int d^3x e^{-i\boldsymbol{p}\cdot\boldsymbol{x}}\langle\psi_\alpha(x)\bar{\Psi}_\beta(0)\rangle \stackrel{\star}{=} Z_l\frac{e^{-E_{\boldsymbol{p}}x_0}}{2E_{\boldsymbol{p}}}\sum_s u^s_\alpha(\boldsymbol{p})\bar{U}^s_\beta(\boldsymbol{p}). \tag{A7}$$

[6]In this Appendix, we use the conventions of Peskin and Schroeder in Minkowski space (with Dirac matrices γ^μ_M) and introduce a corresponding set of Euclidean Dirac matrices, $\gamma_0 = \gamma^0_M$ and $\gamma_k = -i\gamma^k_M$. The γ_μ are all Hermitian; γ_0, γ_2, and γ_5 are symmetric, and γ_1 and γ_3 are antisymmetric.

We now define

$$\mathcal{M}(\boldsymbol{p}) \equiv \sum_s U^s(\boldsymbol{p})\bar{u}^s(\boldsymbol{p}). \tag{A8}$$

The other spin sums can also be expressed through $\mathcal{M}$. First, we have

$$\sum_s u^s(\boldsymbol{p})\bar{U}^s(\boldsymbol{p}) = \gamma_0\mathcal{M}(\boldsymbol{p})^\dagger\gamma_0. \tag{A9}$$

Since the overlap of the local nucleon operator is a genuine Dirac spinor, the matrix $\mathcal{M}$ satisfies

$$\mathcal{M}(\boldsymbol{p})(\gamma_0 E_{\boldsymbol{p}} - i\boldsymbol{p}\cdot\boldsymbol{\gamma} - m_N) = 0. \tag{A10}$$

We observe from the definition of $\mathcal{M}$ that

$$\mathcal{M}(\boldsymbol{p})u^s(\boldsymbol{p}) = 2m_N U^s(\boldsymbol{p}), \tag{A11}$$

and hence also

$$\bar{U}^s(\boldsymbol{p}) = \frac{1}{2m_N}\bar{u}^s(\boldsymbol{p})\gamma_0\mathcal{M}(\boldsymbol{p})^\dagger\gamma_0. \tag{A12}$$

We can thus write the spin sum appearing in the two-point function $C_{2,ss}$ as

$$\sum_s U^s(\boldsymbol{p})\bar{U}^s(\boldsymbol{p}) = \frac{1}{4m_N^2}\mathcal{M}(\boldsymbol{p})(E_{\boldsymbol{p}}\gamma_0 - i\boldsymbol{p}\cdot\boldsymbol{\gamma} + m_N) \times \gamma_0\mathcal{M}(\boldsymbol{p})^\dagger\gamma_0 \tag{A13}$$

$$= \frac{1}{2m_N}\mathcal{M}(\boldsymbol{p})\gamma_0\mathcal{M}(\boldsymbol{p})^\dagger\gamma_0. \tag{A14}$$

The second equality uses Eq. (A10). Thus, γ_0 times the spin sum of the U's is a Hermitian matrix.

Let $J(x)$ be a local operator with the following matrix elements between one-nucleon states[7]:

$$\langle N,\boldsymbol{p}',s'|J(0)|N,\boldsymbol{p},s\rangle = \bar{u}^{s'}(\boldsymbol{p}')\mathcal{J}(\boldsymbol{q})u^s(\boldsymbol{p}), \tag{A15}$$

where $\boldsymbol{q} \equiv \boldsymbol{p}' - \boldsymbol{p}$. The three-point function relevant to form factor calculations with a vanishing momentum at the sink and its spectral representation read (for $x_0 > y_0 > 0$)

[7]For instance, $\mathcal{J}(\boldsymbol{q}) = (\gamma^\mu_M F_1(q^2) + i\sigma^{\mu\nu}_M\frac{q_\nu}{2m_N}F_2(q^2))$ ($\sigma^{\mu\nu}_M \equiv \frac{i}{2}[\gamma^\mu_M,\gamma^\nu_M]$) for the vector current $\bar{\psi}(x)\gamma^\mu_M\psi(x)$.

$$C^{\alpha\beta}_{3,J}(\boldsymbol{q}, y_0, x_0) \equiv \int d^3y \int d^3x e^{+i\boldsymbol{q}\cdot\boldsymbol{y}} \langle \Psi_\alpha(x) J(y) \bar{\Psi}_\beta(0)\rangle$$
$$\stackrel{\star}{=} \frac{e^{-E_{\boldsymbol{q}} y_0}}{2E_{\boldsymbol{q}}} \frac{e^{-m(x_0-y_0)}}{2m_N} \left(\sum_{s'} U^{s'}_\alpha(\boldsymbol{0}) \bar{u}^{s'}_\gamma(\boldsymbol{0})\right)$$
$$\times (\mathcal{J}(\boldsymbol{q}))_{\gamma\delta} \left(\sum_s u^s_\delta(-\boldsymbol{q}) \bar{U}^s_\beta(-\boldsymbol{q})\right). \tag{A16}$$

The three-point function, projected with a generic projector Γ,

$$\mathrm{Tr}\{\Gamma C_3(\boldsymbol{q}, y_0, x_0)\}$$
$$\stackrel{\star}{=} \frac{e^{-E_{\boldsymbol{q}} y_0}}{2E_{\boldsymbol{q}}} \frac{e^{-m(x_0-y_0)}}{2m_N} \mathrm{Tr}\{\Gamma \mathcal{M}(\boldsymbol{0}) \mathcal{J}(\boldsymbol{q}) \gamma_0 \mathcal{M}(-\boldsymbol{q})^\dagger \gamma_0\} \tag{A17}$$

can thus also be expressed in terms of the matrix $\mathcal{M}(\boldsymbol{p})$. The latter can be expanded in the 16 linearly independent spinor-space matrices, and symmetries can be used to restrict the terms that contribute.

1. Symmetry constraints on nucleon two-point functions

Let

$$C_{2,\phi\chi}(\boldsymbol{p}, x_0) \equiv \int d^3x e^{-i\boldsymbol{p}\cdot\boldsymbol{x}} \langle \phi(x) \bar{\chi}(0)\rangle \tag{A18}$$

be a generic nucleon two-point function with interpolating operators ϕ and χ. We assume that the latter are good spinors with respect to spatial rotations and with respect to all discrete symmetries, but no assumption is made on their behavior under boosts. The implications of the various symmetries are:

(i) rotation invariance:

$$C_{2,\phi\chi}(R\boldsymbol{p}, x_0) = \Lambda_{\frac{1}{2}}(R) C_{2,\phi\chi}(\boldsymbol{p}, x_0) \Lambda_{\frac{1}{2}}(R)^{-1}, \tag{A19}$$

where $\phi(x) \to \Lambda_{\frac{1}{2}}(R)\phi(R^{-1}x)$ is the transformation law of the quark fields;

(ii) parity:

$$C_{2,\phi\chi}(-\boldsymbol{p}, x_0) = \gamma_0 C_{2,\phi\chi}(\boldsymbol{p}, x_0)\gamma_0; \tag{A20}$$

(iii) Euclidean time reversal:

$$C_{2,\phi\chi}(\boldsymbol{p}, -x_0) = \gamma_0\gamma_5 C_{2,\phi\chi}(\boldsymbol{p}, x_0)\gamma_5\gamma_0; \tag{A21}$$

(iv) charge conjugation: assuming that the nucleon interpolating fields transform like the quark fields $[q_\alpha(x) \to (\bar{q}(x)\gamma_0\gamma_2)_\alpha,\ \bar{q}_\alpha(x) \to (\gamma_0\gamma_2 q(x))_\alpha]$[8]

$$C_{2,\phi\chi}(-\boldsymbol{p}, -x_0)^\top = \gamma_2\gamma_0 C_{2,\chi\phi}(\boldsymbol{p}, x_0)\gamma_0\gamma_2. \tag{A22}$$

Combining the three discrete symmetries, we obtain, for later use,

$$\gamma_5 C_{2,\phi\chi}(\boldsymbol{p}, x_0)^\top \gamma_5 = \gamma_2\gamma_0 C_{2,\chi\phi}(\boldsymbol{p}, x_0)\gamma_0\gamma_2. \tag{A23}$$

The most general form of the nucleon two-point functions allowed by rotation symmetry and parity is

$$C_{2,\phi\chi}(\boldsymbol{p}, x_0) = \mathcal{F}_s(\boldsymbol{p}^2, x_0) + \mathcal{F}_0(\boldsymbol{p}^2, x_0)\gamma_0$$
$$- i\mathcal{F}_V(\boldsymbol{p}^2, x_0)\boldsymbol{p}\cdot\boldsymbol{\gamma} - i\mathcal{F}_T(\boldsymbol{p}^2, x_0)\gamma_0\boldsymbol{p}\cdot\boldsymbol{\gamma}. \tag{A24}$$

Time-reversal invariance implies that $\mathcal{F}_0$ and $\mathcal{F}_T$ are odd functions of x_0, while $\mathcal{F}_s$ and $\mathcal{F}_V$ are even functions of x_0. Charge conjugation relates the functions $\mathcal{F}$ parametrizing the correlator $C_{2,\phi\chi}$ to those parametrizing the correlator $C_{2,\chi\phi}$.

2. General parametrization of $\mathcal{M}(p)$

In view of (A24), we parametrize $\mathcal{M}(\boldsymbol{p})$ as

$$\mathcal{M}(\boldsymbol{p}) = m_N f_s(\boldsymbol{p}^2) + f_0(\boldsymbol{p}^2)E_{\boldsymbol{p}}\gamma_0 - i f_V(\boldsymbol{p}^2)\boldsymbol{p}\cdot\boldsymbol{\gamma}$$
$$- i f_T(\boldsymbol{p}^2)\boldsymbol{p}\cdot(\gamma_0\boldsymbol{\gamma}). \tag{A25}$$

The condition (A10) from the spectral representation implies the constraints

$$f_V(\boldsymbol{p}^2) = \frac{1}{\boldsymbol{p}^2}(E^2_{\boldsymbol{p}} f_0(\boldsymbol{p}^2) - m_N^2 f_s(\boldsymbol{p}^2)), \tag{A26}$$

$$f_T(\boldsymbol{p}^2) = \frac{m_N E_{\boldsymbol{p}}}{\boldsymbol{p}^2}(f_s(\boldsymbol{p}^2) - f_0(\boldsymbol{p}^2)). \tag{A27}$$

In particular, $f_0(\boldsymbol{p}^2) - f_s(\boldsymbol{p}^2) = \mathrm{O}(\boldsymbol{p}^2)$; the case of a Lorentz-covariant spinor source corresponds to $f_0 = f_s = f_V$ independent of $\boldsymbol{p}$ and $f_T = 0$ identically. Now, combining the discrete-symmetry property (A23) and the spectral representations (A6), (A7), one derives the property that f_0, f_s, f_V, and f_T must all be real-valued functions.

It is convenient to decompose $\mathcal{M}$ as follows:

$$\mathcal{M}(\boldsymbol{p}) = \mathcal{M}_+(\boldsymbol{p}) + \mathcal{M}_-(\boldsymbol{p}), \tag{A28}$$

$$\mathcal{M}_\pm(\boldsymbol{p}) = \frac{1}{2}(1 \pm \gamma_0)\mathcal{M}(\boldsymbol{p}). \tag{A29}$$

[8]This condition fixes the phase of the interpolating fields. An interpolating field that satisfies this condition is $\chi_\alpha(x) = \epsilon^{abc}(u^a_\beta(\gamma_0\gamma_2\gamma_5)_{\beta\gamma}d^b_\gamma)u^c_\alpha$, but $e^{i\varphi}\chi_\alpha(x)$ does not for $\varphi \neq 0, \pi$.

Using the constraints, one finds the following general form of $\mathcal{M}_\pm(\boldsymbol{p})$:

$$\mathcal{M}_+(\boldsymbol{p}) = \frac{1}{2}(1+\gamma_0)Z_+(\boldsymbol{p})(E_{\boldsymbol{p}} + m_N - i\boldsymbol{p}\cdot\boldsymbol{\gamma}), \quad \text{(A30)}$$

$$\mathcal{M}_-(\boldsymbol{p}) = \frac{1}{2}(1-\gamma_0)Z_-(\boldsymbol{p})(E_{\boldsymbol{p}} - m_N + i\boldsymbol{p}\cdot\boldsymbol{\gamma}) \quad \text{(A31)}$$

with the relations

$$Z_+(\boldsymbol{p}) = \frac{m_N f_s(\boldsymbol{p}^2) + E_{\boldsymbol{p}} f_0(\boldsymbol{p}^2)}{E_{\boldsymbol{p}} + m_N}, \quad \text{(A32)}$$

$$Z_-(\boldsymbol{p}) = \frac{m_N f_s(\boldsymbol{p}^2) - E_{\boldsymbol{p}} f_0(\boldsymbol{p}^2)}{E_{\boldsymbol{p}} - m_N}. \quad \text{(A33)}$$

The bottom line is that the matrix $\mathcal{M}(\boldsymbol{p})$ is parametrized by two (spatially scalar) functions $Z_\pm(\boldsymbol{p})$, which are linear functions of the nucleon interpolating operator $\Psi_\alpha(x)$. Its phase can be chosen such that $Z_\pm(\boldsymbol{p})$ are real for all $\boldsymbol{p}$. Furthermore, it can be chosen such that $Z_+(\boldsymbol{p}=0)$ is positive. The generic case that we will consider is then that it remains positive for all momenta.[9] As a side remark, we note that in the rest frame only parity-odd states (not considered here) contribute to $\mathrm{Tr}\{(1-\gamma_0)C_{2,sl}(\boldsymbol{p}=0,x_0)\}$.

3. Final form of the noncovariant two-point and three-point functions

We now specialize to the projector

$$\Gamma = \frac{1}{2}(1+\gamma_0)(1+i\gamma_5\gamma_3). \quad \text{(A34)}$$

Starting from Eqs. (A5) and (A13), the projected two-point function can be written[10]

$$\begin{aligned}\mathrm{Tr}\{\Gamma C_{2,ss}(\boldsymbol{p},x_0)\} &\overset{\star}{=} \frac{e^{-E_p x_0}}{2E_{\boldsymbol{p}}}\cdot\frac{1}{2m_N}\mathrm{Tr}\{(1+i\gamma_5\gamma_3)\\ &\quad\times\mathcal{M}_+(\boldsymbol{p})\gamma_0\mathcal{M}_+(\boldsymbol{p})^\dagger\gamma_0\}\\ &= |Z_+(\boldsymbol{p})|^2(1+m_N/E_{\boldsymbol{p}})e^{-E_{\boldsymbol{p}}x_0}. \quad \text{(A35)}\end{aligned}$$

The second equality uses the parametrization Eq. (A30). The term $i\gamma_5\gamma_3$ in Γ_p does not contribute to this expression. The trace appearing in Eq. (A17) takes the form

$$\begin{aligned}&\mathrm{Tr}\{\Gamma_p\mathcal{M}(\boldsymbol{0})\mathcal{J}(\boldsymbol{q})\gamma_0\mathcal{M}(-\boldsymbol{q})^\dagger\gamma_0\}\\ &\quad= \mathrm{Tr}\{(1+i\gamma_5\gamma_3)\mathcal{M}_+(\boldsymbol{0})\mathcal{J}(\boldsymbol{q})\gamma_0\mathcal{M}_+(-\boldsymbol{q})^\dagger\}. \quad \text{(A36)}\end{aligned}$$

Thus, the expression for the three-point function becomes

$$\begin{aligned}&C_3(\boldsymbol{q},y_0,x_0)\\ &\quad\overset{\star}{=} \frac{e^{-E_q y_0}}{2E_{\boldsymbol{q}}}\frac{e^{-m_N(x_0-y_0)}}{2m_N}Z_+(0)Z_+(-\boldsymbol{q})^*\\ &\qquad\times m_N\mathrm{Tr}\{(1+\gamma_0)(1+i\gamma_5\gamma_3)\mathcal{J}(\boldsymbol{q})\\ &\qquad\times(m_N + E_{\boldsymbol{q}} + i\boldsymbol{q}\cdot\boldsymbol{\gamma})\}. \quad \text{(A37)}\end{aligned}$$

As we have seen, the phase of the nucleon interpolating operator $\Psi(x)$ can be chosen such that $Z_+(\boldsymbol{p}) > 0$ for all $\boldsymbol{p}$. If the phase had not been chosen in this way, the common phase would nonetheless cancel in the product $Z_+(0)Z_+(-\boldsymbol{q})^*$.

For a covariant source, the result would be identical to (A37), except that $Z_+(\boldsymbol{p})$ would be independent of $\boldsymbol{p}$. In the standard expression of the ratio (13), the three-point function is, however, divided by the appropriate combination of two-point functions to cancel the overlap factor $Z_+(\boldsymbol{p})$ for each value of $\boldsymbol{p}$. The correctness of our calculation is thus not affected by the use of noncovariant interpolating operators.

APPENDIX B: Q^2 TABLES

In Tables VI–XVI, we give all of our results for the isovector vector form factors G_E and G_M of the nucleon at all values of Q^2 measured on each ensemble. Listed in each case are the values obtained using the plateau method with a source-sink separation of $t_s = 1.1$ fm, the summation method, and an explicit two-state fit (cf. the main text for details). The statistical errors on each data point are quoted in parentheses following the central value.

[9] *A priori*, it could happen that it becomes negative for some momenta, but then by continuity it would have to vanish somewhere, and there is no symmetry reason for this to happen.

[10] In the following equations, we allow for the case that the $Z_+(\boldsymbol{p})$ have a common phase for all $\boldsymbol{p}$.

TABLE VI. A3 ensemble ($a = 0.079$ fm, $m_\pi = 473$ MeV): vector form factors at all Q^2 values for all extraction methods.

A3	G_E			G_M		
Q^2 (GeV^2)	Plat (1.1 fm)	Summation	Two-state	Plat (1.1 fm)	Summation	Two-state
0.230	0.752 (0.011)	0.725 (0.018)	0.734 (0.012)	3.040 (0.100)	3.320 (0.175)	3.067 (0.128)
0.443	0.601 (0.013)	0.583 (0.025)	0.592 (0.017)	2.359 (0.078)	2.503 (0.147)	2.272 (0.111)
0.639	0.495 (0.018)	0.480 (0.037)	0.484 (0.022)	1.921 (0.084)	1.869 (0.176)	1.783 (0.125)
0.823	0.373 (0.023)	0.322 (0.056)	0.369 (0.036)	1.579 (0.098)	1.716 (0.216)	1.536 (0.158)
0.995	0.331 (0.023)	0.299 (0.055)	0.320 (0.030)	1.349 (0.091)	1.416 (0.205)	1.253 (0.143)
1.156	0.283 (0.031)	0.228 (0.073)	0.213 (0.037)	1.194 (0.121)	0.881 (0.295)	0.910 (0.162)

TABLE VII. A4 ensemble ($a = 0.079$ fm, $m_\pi = 364$ MeV): vector form factors at all Q^2 values for all extraction methods.

A4	G_E			G_M		
Q^2 (GeV^2)	Plat (1.1 fm)	Summation	Two-state	Plat (1.1 fm)	Summation	Two-state
0.229	0.720 (0.024)	0.685 (0.037)	0.668 (0.021)	2.806 (0.147)	2.603 (0.232)	2.726 (0.239)
0.437	0.547 (0.022)	0.466 (0.043)	0.489 (0.031)	2.121 (0.109)	2.360 (0.210)	2.518 (0.210)
0.628	0.459 (0.024)	0.380 (0.048)	0.385 (0.045)	1.936 (0.130)	2.166 (0.199)	2.146 (0.246)
0.805	0.401 (0.039)	0.397 (0.087)	0.339 (0.076)	1.591 (0.239)	1.499 (0.339)	1.408 (0.375)
0.970	0.338 (0.025)	0.338 (0.080)	0.291 (0.052)	1.317 (0.128)	1.449 (0.281)	1.594 (0.262)
1.123	0.299 (0.035)	0.242 (0.099)	0.205 (0.077)	1.046 (0.156)	1.192 (0.352)	1.510 (0.409)

TABLE VIII. A5 ensemble ($a = 0.079$ fm, $m_\pi = 316$ MeV): vector form factors at all Q^2 values for all extraction methods.

A5	G_E			G_M		
Q^2 (GeV^2)	Plat (1.1 fm)	Summation	Two-state	Plat (1.1 fm)	Summation	Two-state
0.228	0.692 (0.018)	0.651 (0.036)	0.629 (0.039)	2.572 (0.159)	2.619 (0.270)	2.672 (0.349)
0.434	0.521 (0.019)	0.461 (0.038)	0.433 (0.040)	1.967 (0.121)	2.082 (0.203)	2.021 (0.272)
0.623	0.424 (0.029)	0.305 (0.058)	0.328 (0.054)	1.720 (0.134)	2.115 (0.277)	1.408 (0.328)
0.797	0.343 (0.043)	0.269 (0.096)	0.171 (0.087)	1.247 (0.158)	0.673 (0.426)	1.430 (0.442)
0.959	0.255 (0.033)	0.176 (0.084)	0.002 (0.075)	1.023 (0.135)	0.989 (0.350)	0.867 (0.381)
1.110	0.065 (0.093)	0.189 (0.114)	0.067 (0.128)	0.760 (0.340)	0.750 (0.523)	-0.338 (0.522)

TABLE IX. B6 ensemble ($a = 0.079$ fm, $m_\pi = 268$ MeV): vector form factors at all Q^2 values for all extraction methods.

B6	G_E			G_M		
Q^2 (GeV^2)	Plat (1.1 fm)	Summation	Two-state	Plat (1.1 fm)	Summation	Two-state
0.104	0.826 (0.008)	0.785 (0.023)	0.760 (0.018)	3.264 (0.121)	3.692 (0.370)	3.794 (0.284)
0.203	0.709 (0.012)	0.664 (0.036)	0.669 (0.025)	2.819 (0.121)	3.172 (0.258)	2.571 (0.260)
0.297	0.622 (0.017)	0.572 (0.048)	0.541 (0.038)	2.312 (0.121)	2.417 (0.245)	2.283 (0.299)
0.387	0.565 (0.018)	0.569 (0.069)	0.474 (0.042)	2.154 (0.132)	2.435 (0.241)	2.115 (0.300)
0.474	0.507 (0.018)	0.460 (0.053)	0.428 (0.044)	2.034 (0.105)	2.149 (0.216)	1.970 (0.247)
0.557	0.445 (0.020)	0.421 (0.059)	0.374 (0.056)	1.656 (0.069)	1.680 (0.208)	1.399 (0.233)

TABLE X. E5 ensemble ($a = 0.063$ fm, $m_\pi = 457$ MeV): vector form factors at all Q^2 values for all extraction methods.

E5	G_E			G_M		
Q^2 (GeV^2)	Plat (1.1 fm)	Summation	Two-state	Plat (1.1 fm)	Summation	Two-state
0.356	0.663 (0.013)	0.635 (0.018)	0.601 (0.014)	2.611 (0.105)	2.544 (0.150)	2.540 (0.139)
0.675	0.477 (0.016)	0.443 (0.025)	0.411 (0.018)	1.909 (0.090)	1.773 (0.130)	1.782 (0.111)
0.966	0.379 (0.026)	0.357 (0.039)	0.339 (0.029)	1.429 (0.104)	1.346 (0.161)	1.350 (0.151)
1.233	0.209 (0.077)	0.197 (0.065)	0.204 (0.049)	1.342 (0.358)	1.015 (0.242)	1.016 (0.210)
1.480	0.220 (0.046)	0.191 (0.060)	0.190 (0.038)	0.996 (0.178)	0.887 (0.242)	0.929 (0.172)
1.709	0.204 (0.086)	0.164 (0.082)	0.185 (0.054)	0.454 (0.301)	0.644 (0.301)	0.876 (0.241)

TABLE XI. F6 ensemble ($a = 0.063$ fm, $m_\pi = 324$ MeV): vector form factors at all Q^2 values for all extraction methods.

F6	G_E			G_M		
Q^2 (GeV^2)	Plat (1.1 fm)	Summation	Two-state	Plat (1.1 fm)	Summation	Two-state
0.162	0.766 (0.009)	0.746 (0.011)	0.725 (0.009)	2.834 (0.125)	2.963 (0.143)	2.586 (0.216)
0.314	0.627 (0.012)	0.604 (0.015)	0.555 (0.014)	2.410 (0.102)	2.350 (0.116)	2.128 (0.166)
0.457	0.541 (0.016)	0.516 (0.019)	0.455 (0.020)	2.028 (0.103)	1.809 (0.128)	1.962 (0.173)
0.593	0.423 (0.017)	0.394 (0.023)	0.332 (0.027)	1.586 (0.084)	1.505 (0.116)	1.474 (0.199)
0.723	0.383 (0.017)	0.343 (0.024)	0.307 (0.025)	1.435 (0.072)	1.245 (0.111)	1.306 (0.165)
0.846	0.342 (0.021)	0.291 (0.028)	0.253 (0.030)	1.278 (0.076)	1.007 (0.133)	1.205 (0.171)

TABLE XII. F7 ensemble ($a = 0.063$ fm, $m_\pi = 277$ MeV): vector form factors at all Q^2 values for all extraction methods.

F7	G_E			G_M		
Q^2 (GeV^2)	Plat (1.1 fm)	Summation	Two-state	Plat (1.1 fm)	Summation	Two-state
0.162	0.759 (0.013)	0.751 (0.016)	0.723 (0.017)	2.894 (0.167)	3.106 (0.192)	2.637 (0.329)
0.313	0.623 (0.020)	0.612 (0.020)	0.566 (0.025)	2.383 (0.136)	2.462 (0.158)	1.893 (0.258)
0.455	0.512 (0.026)	0.507 (0.027)	0.421 (0.033)	1.944 (0.111)	2.065 (0.158)	1.613 (0.294)
0.589	0.442 (0.026)	0.410 (0.033)	0.270 (0.048)	1.706 (0.130)	1.649 (0.175)	1.284 (0.307)
0.717	0.417 (0.037)	0.372 (0.031)	0.289 (0.048)	1.461 (0.107)	1.465 (0.141)	1.336 (0.302)
0.838	0.336 (0.036)	0.308 (0.038)	0.200 (0.051)	1.295 (0.126)	1.329 (0.165)	0.911 (0.342)

TABLE XIII. G8 ensemble ($a = 0.063$ fm, $m_\pi = 193$ MeV): vector form factors at all Q^2 values for all extraction methods.

G8	G_E			G_M		
Q^2 (GeV^2)	Plat (1.1 fm)	Summation	Two-state	Plat (1.1 fm)	Summation	Two-state
0.092	0.870 (0.013)	0.928 (0.041)	0.771 (0.030)	3.367 (0.243)	4.272 (0.618)	4.555 (0.815)
0.181	0.731 (0.014)	0.737 (0.046)	0.563 (0.040)	2.822 (0.160)	3.293 (0.398)	3.081 (0.546)
0.266	0.629 (0.016)	0.591 (0.055)	0.396 (0.060)	2.464 (0.155)	2.972 (0.383)	2.879 (0.600)
0.347	0.558 (0.022)	0.510 (0.071)	0.292 (0.074)	2.173 (0.131)	3.088 (0.410)	2.168 (0.568)
0.426	0.499 (0.018)	0.473 (0.058)	0.149 (0.065)	1.902 (0.119)	2.311 (0.315)	1.862 (0.483)
0.503	0.458 (0.020)	0.419 (0.068)	0.048 (0.082)	1.688 (0.130)	1.899 (0.370)	1.767 (0.492)

TABLE XIV. N5 ensemble ($a = 0.050$ fm, $m_\pi = 429$ MeV): vector form factors at all Q^2 values for all extraction methods.

N5	G_E			G_M		
Q^2 (GeV^2)	Plat (1.1 fm)	Summation	Two-state	Plat (1.1 fm)	Summation	Two-state
0.257	0.708 (0.008)	0.678 (0.018)	0.687 (0.008)	2.858 (0.086)	2.703 (0.164)	2.768 (0.101)
0.494	0.551 (0.010)	0.509 (0.023)	0.504 (0.011)	2.171 (0.063)	2.082 (0.129)	2.105 (0.083)
0.715	0.445 (0.014)	0.414 (0.032)	0.386 (0.016)	1.763 (0.067)	1.697 (0.158)	1.639 (0.094)
0.922	0.397 (0.021)	0.331 (0.049)	0.299 (0.021)	1.627 (0.090)	1.129 (0.196)	1.214 (0.111)
1.118	0.332 (0.019)	0.275 (0.044)	0.252 (0.018)	1.310 (0.077)	1.204 (0.176)	1.028 (0.085)
1.303	0.278 (0.025)	0.215 (0.061)	0.190 (0.023)	1.117 (0.097)	0.939 (0.242)	0.789 (0.103)

TABLE XV. N6 ensemble ($a = 0.050$ fm, $m_\pi = 331$ MeV): vector form factors at all Q^2 values for all extraction methods.

N6	G_E			G_M		
Q^2 (GeV^2)	Plat (1.1 fm)	Summation	Two-state	Plat (1.1 fm)	Summation	Two-state
0.255	0.681 (0.011)	0.644 (0.012)	0.588 (0.012)	2.618 (0.096)	2.797 (0.107)	2.452 (0.149)
0.487	0.512 (0.013)	0.473 (0.014)	0.373 (0.015)	2.004 (0.071)	2.083 (0.083)	1.717 (0.124)
0.701	0.386 (0.017)	0.344 (0.020)	0.235 (0.025)	1.433 (0.070)	1.688 (0.091)	1.236 (0.144)
0.900	0.363 (0.026)	0.331 (0.031)	0.173 (0.036)	1.341 (0.102)	1.754 (0.127)	1.177 (0.202)
1.087	0.282 (0.018)	0.271 (0.026)	0.152 (0.030)	1.041 (0.068)	1.090 (0.101)	0.724 (0.158)
1.264	0.222 (0.021)	0.204 (0.033)	0.120 (0.039)	0.763 (0.071)	0.876 (0.128)	0.390 (0.181)

TABLE XVI. O7 ensemble ($a = 0.050$ fm, $m_\pi = 261$ MeV): vector form factors at all Q^2 values for all extraction methods.

O7	G_E			G_M		
Q^2 (GeV^2)	Plat (1.1 fm)	Summation	Two-state	Plat (1.1 fm)	Summation	Two-state
0.146	0.786 (0.010)	0.773 (0.012)	0.700 (0.017)	2.800 (0.126)	2.825 (0.139)	2.886 (0.259)
0.282	0.648 (0.013)	0.618 (0.015)	0.485 (0.021)	2.230 (0.096)	2.299 (0.118)	1.976 (0.205)
0.411	0.554 (0.015)	0.521 (0.019)	0.357 (0.026)	1.929 (0.086)	1.964 (0.111)	1.449 (0.211)
0.533	0.474 (0.018)	0.401 (0.022)	0.231 (0.035)	1.743 (0.100)	1.589 (0.111)	1.059 (0.239)
0.650	0.428 (0.017)	0.351 (0.023)	0.172 (0.033)	1.445 (0.075)	1.387 (0.096)	0.755 (0.194)
0.761	0.388 (0.019)	0.327 (0.029)	0.176 (0.033)	1.249 (0.070)	1.266 (0.096)	0.662 (0.210)

[1] C. Perdrisat, V. Punjabi, and M. Vanderhaeghen, Prog. Part. Nucl. Phys. **59**, 694 (2007).
[2] J. Bernauer *et al.* (A1 Collaboration), Phys. Rev. Lett. **105**, 242001 (2010).
[3] J. Bernauer *et al.* (A1 Collaboration), Phys. Rev. C **90**, 015206 (2014).
[4] M. Jones *et al.* (Jefferson Lab Hall A Collaboration), Phys. Rev. Lett. **84**, 1398 (2000).
[5] O. Gayou *et al.* (Jefferson Lab Hall A Collaboration), Phys. Rev. Lett. **88**, 092301 (2002).
[6] V. Punjabi *et al.*, Phys. Rev. C **71**, 055202 (2005).
[7] A. Puckett *et al.*, Phys. Rev. Lett. **104**, 242301 (2010).
[8] R. Pohl *et al.*, Nature (London) **466**, 213 (2010).
[9] A. Antognini *et al.*, Science **339**, 417 (2013).
[10] P. J. Mohr, B. N. Taylor, and D. B. Newell, Rev. Mod. Phys. **84**, 1527 (2012).
[11] C. Alexandrou, G. Koutsou, J. W. Negele, and A. Tsapalis, Phys. Rev. D **74**, 034508 (2006).
[12] H.-W. Lin, T. Blum, S. Ohta, S. Sasaki, and T. Yamazaki, Phys. Rev. D **78**, 014505 (2008).
[13] T. Yamazaki, Y. Aoki, T. Blum, H.-Wen Lin, S. Ohta, S. Sasaki, R. Tweedie, and J. Zanotti, Phys. Rev. D **79**, 114505 (2009).
[14] S. Syritsyn *et al.*, Phys. Rev. D **81**, 034507 (2010).

[15] M. Göckeler *et al.* (QCDSF/UKQCD Collaboration), *Proc. Sci.*, LATTICE2009 (2009) 125.
[16] J. Bratt *et al.* (LHPC Collaboration), Phys. Rev. D **82**, 094502 (2010).
[17] D. Pleiter *et al.* (QCDSF/UKQCD Collaboration), *Proc. Sci.*, LATTICE2010 (2010) 153.
[18] C. Alexandrou, M. Brinet, J. Carbonell, M. Constantinou, P. A. Harraud, P. Guichon, K. Jansen, T. Korzec, and M. Papinutto, Phys. Rev. D **83**, 094502 (2011).
[19] M. Göckeler *et al.* (QCDSF/UKQCD Collaboration), *Proc. Sci.*, LATTICE2010 (2010) 163.
[20] S. Collins *et al.*, Phys. Rev. D **84**, 074507 (2011).
[21] J. Green *et al.*, *Proc. Sci.*, LATTICE2013 (2014) 276.
[22] B. Jäger *et al.*, *Proc. Sci.*, LATTICE2013 (2014) 272.
[23] J. R. Green, J. W. Negele, A. V. Pochinsky, S. N. Syritsyn, M. Engelhardt, and S. Krieg, Phys. Rev. D **90**, 074507 (2014).
[24] S. Güsken, Nucl. Phys. B, Proc. Suppl. **17**, 361 (1990).
[25] L. Maiani, G. Martinelli, M. Paciello, and B. Taglienti, Nucl. Phys. **B293**, 420 (1987).
[26] T. Doi, M. Deka, S.-J. Dong, T. Draper, Keh-Fei Liu, D. Mankame, N. Mathur, and T. Streuer, Phys. Rev. D **80**, 094503 (2009).
[27] S. Capitani, M. Della Morte, G. von Hippel, B. Jäger, A. Jüttner, B. Knippschild, H. B. Meyer, and H. Wittig, Phys. Rev. D **86**, 074502 (2012).
[28] G. Colangelo *et al.*, Eur. Phys. J. C **71**, 1695 (2011).
[29] T. Becher and H. Leutwyler, Eur. Phys. J. C **9**, 643 (1999).
[30] B. Kubis and U.-G. Meißner, Nucl. Phys. **A679**, 698 (2001).
[31] T. Fuchs, J. Gegelia, G. Japaridze, and S. Scherer, Phys. Rev. D **68**, 056005 (2003).
[32] T. Bauer, J. Bernauer, and S. Scherer, Phys. Rev. C **86**, 065206 (2012).
[33] M. Rosenbluth, Phys. Rev. **79**, 615 (1950).
[34] C. Alexandrou *et al.* (ETM Collaboration), *Proc. Sci.*, LATTICE2008 (2008) 139.
[35] K. Jansen and R. Sommer (ALPHA Collaboration), Nucl. Phys. **B530**, 185 (1998).
[36] M. Lüscher, Comput. Phys. Commun. **165**, 199 (2005).
[37] M. Lüscher, J. High Energy Phys. 12 (2007) 011.
[38] M. Marinkovic and S. Schaefer, *Proc. Sci.*, LATTICE2010 (2010) 031.
[39] M. Lüscher, S. Sint, R. Sommer, and P. Weisz, Nucl. Phys. **B478**, 365 (1996).
[40] M. Della Morte, R. Hoffmann, F. Knechtli, R. Sommer, and U. Wolff, J. High Energy Phys. 07 (2005) 007.
[41] M. Della Morte, R. Sommer, and S. Takeda, Phys. Lett. B **672**, 407 (2009).
[42] S. Güsken, U. Löw, K.-H. Mütter, R. Sommer, A. Patel, and K. Schilling, Phys. Lett. B **227**, 266 (1989).
[43] M. Albanese *et al.* (APE Collaboration), Phys. Lett. B **192**, 163 (1987).
[44] G. M. von Hippel, B. Jäger, T. D. Rae, and H. Wittig, J. High Energy Phys. 09 (2013) 014.
[45] M. Della Morte, B. Jäger, T. Rae, and H. Wittig, Eur. Phys. J. A **48**, 139 (2012).
[46] G. Martinelli and C. T. Sachrajda, Nucl. Phys. **B316**, 355 (1989).
[47] S. Capitani, M. Della Morte, G. von Hippel, B. Knippschild, and H. Wittig, *Proc. Sci.*, LATTICE2011 (2011) 145.
[48] P. Fritzsch, F. Knechtli, B. Leder, M. Marinkovic, S. Schaefer, R. Sommer, and F. Virotta, Nucl. Phys. **B865**, 397 (2012).
[49] S. Lottini, *Proc. Sci.*, LATTICE2013 (2013) 315.
[50] M. Lüscher and S. Schaefer, J. High Energy Phys. 07 (2011) 036.
[51] S. Schaefer, R. Sommer, and F. Virotta (ALPHA Collaboration), Nucl. Phys. **B845**, 93 (2011).
[52] G. Parisi, Phys. Rep. **103**, 203 (1984).
[53] G. P. Lepage, *Theoretical Advanced Study Institute in Elementary-particle Physics (TASI '89)*, edited by T. A. DeGrand and D. Toussaint (World Scientific, Singapore, 1990), p. 97.
[54] J. Bulava, M. Donnellan, and R. Sommer, J. High Energy Phys. 01 (2012) 140.
[55] B. B. Brandt, S. Capitani, M. Della Morte, D. Djukanovic, J. Gegelia, G. von Hippel, A. Jüttner, B. Knippschild, H. B. Meyer, and H. Wittig, Eur. Phys. J. Spec. Top. **198**, 79 (2011).
[56] J. R. Green, M. Engelhardt, S. Krieg, J. W. Negele, A. V. Pochinsky, and S. N. Syritsyn, Phys. Lett. B **734**, 290 (2014).
[57] J. Kelly, Phys. Rev. C **70**, 068202 (2004).
[58] J. Arrington and I. Sick, Phys. Rev. C **76**, 035201 (2007).
[59] I. Lorenz, H.-W. Hammer, and U.-G. Meißner, Eur. Phys. J. A **48**, 151 (2012).
[60] E. E. Jenkins and A. V. Manohar, Phys. Lett. B **255**, 558 (1991).
[61] V. Bernard, H. W. Fearing, T. R. Hemmert, and U. G. Meißner, Nucl. Phys. **A635**, 121 (1998).
[62] M. Göckeler, T. R. Hemmert, R. Horsley, D. Pleiter, P. E. L. Rakow, A. Schäfer, and G. Schierholz (QCDSF Collaboration), Phys. Rev. D **71**, 034508 (2005).
[63] T. Ledwig, J. Martin-Camalich, V. Pascalutsa, and M. Vanderhaeghen, Phys. Rev. D **85**, 034013 (2012).
[64] M. R. Schindler, J. Gegelia, and S. Scherer, Eur. Phys. J. A **26**, 1 (2005).
[65] D. Djukanovic, M. Schindler, J. Gegelia, G. Japaridze, and S. Scherer, Phys. Rev. Lett. **93**, 122002 (2004).
[66] K. Kawarabayashi and M. Suzuki, Phys. Rev. Lett. **16**, 255 (1966).
[67] Riazuddin and Fayyazuddin, Phys. Rev. **147**, 1071 (1966).
[68] T. Bauer, diploma thesis, University of Mainz, 2009 (in German), http://portal.kph.uni-mainz.de/T/pub/diploma/Dipl_Th_Bauer.pdf.
[69] T. Hahn and M. Pérez-Victoria, Comput. Phys. Commun. **118**, 153 (1999).
[70] G. van Oldenborgh and J. Vermaseren, Z. Phys. C **46**, 425 (1990).
[71] T. R. Hemmert and W. Weise, Eur. Phys. J. A **15**, 487 (2002).
[72] E. Shintani, R. Arthur, T. Blum, T. Izubuchi, C. Jung, and C. Lehner, Phys. Rev. D **91**, 114511 (2015).
[73] C. Michael and I. Teasdale, Nucl. Phys. **B215**, 433 (1983).
[74] M. Lüscher and U. Wolff, Nucl. Phys. **B339**, 222 (1990).
[75] B. Blossier, M. Della Morte, G. von Hippel, T. Mendes, and R. Sommer, J. High Energy Phys. 04 (2009) 094.
[76] V. Gülpers, G. von Hippel, and H. Wittig, Phys. Rev. D **89**, 094503 (2014).

[77] V. Gülpers, G. von Hippel, and H. Wittig, *Proc. Sci.*, LATTICE2013 (2014) 283.
[78] V. Gülpers, Ph.D. thesis, University of Mainz, 2015.
[79] R. Babich, R. C. Brower, M. A. Clark, G. T. Fleming, J. C. Osborn, C. Rebbi, and D. Schaich, Phys. Rev. D **85**, 054510 (2012).
[80] A. Abdel-Rehim, C. Alexandrou, M. Constantinou, V. Drach, K. Hadjiyiannakou, K. Jansen, G. Koutsou, and A. Vaquero, Phys. Rev. D **89**, 034501 (2014).
[81] R. Gupta, T. Bhattacharya, A. Joseph, H.-W. Lin, and B. Yoon, *Proc. Sci.*, Lattice2014 (2014) 152.